Convective Inhibition, Subgrid-Scale Triggering Energy, and Stratiform Instability in a Toy Tropical Wave Model

BRIAN E. MAPES

NOAA–CIRES Climate Diagnostics Center, Boulder, Colorado

ABSTRACT

A toy model of large-scale deep convection variations is constructed around a radiative–convective equilibrium climate, with an observed mean sounding as its thermodynamic basic state.

Vertical structure is truncated at two modes, excited by convective (one-signed) and stratiform (two-signed) heating processes in tropical deep convection. Separate treatments of deep and shallow convection are justified by observations that deep convection is more variable. Deep convection intensity is assumed to be modulated by convective available potential energy (CAPE), while occurrence frequency is modulated by the ratio of convective inhibition (CIN) to "triggering energy" K, a scalar representing the intensity of subgrid-scale fluctuations. Deep convective downdrafts cool and dry the boundary layer but also increase K. Variations of K make the relationship between convection and thermodynamic variables (CAPE, CIN, θ_e) nonunique and amplify the deep convective response to temperature waves of small ($\sim$1°C) amplitude.

For a parameter set in which CAPE variations control convection, moist convective damping destroys all variability. When CIN/K variations have dominant importance (the "inhibition-controlled" regime), a mechanism termed "stratiform instability" generates large-scale waves. This mechanism involves lower-tropospheric cooling by stratiform precipitation, which preferentially occurs where the already cool lower troposphere favors deep convection, via smaller CIN. Stratiform instability has two subregimes, based on the relative importance of the two opposite effects of downdrafts: When boundary layer θ_e reduction (a local negative feedback) is stronger, small-scale waves with frequency based on the boundary layer recovery time are preferred. When the K-generation effect (positive feedback) is stronger, very large scales (low wavenumbers of the domain) develop. A mixture of these scales occurs for parameter choices based on observations. Model waves resemble observed waves, with a phase speed $\sim$20 m s^{-1} (near the dry wave speed of the second internal mode), and a "cold boomerang" vertical temperature structure.

Although K exhibits "quasi-equilibrium" with other convection variables (correlations > 0.99), replacing the prognostic K equation with diagnostic equations based on these relationships can put the model into wildly different regimes, if small time lags indicative of causality are distorted. The response of model convection to climatological spatial anomalies of θ_e (proxy for SST) and K (proxy for orographic and coastal triggering) is considered. Higher SST tends broadly to favor convection under either CAPE-controlled or inhibition-controlled regimes, but there are dynamical embellishments in the inhibition-controlled regime. The Kelvin wave seems to be the preferred structure when the model is run on a uniform equatorial β plane.

1. Introduction

The tropical troposphere cools by radiation at a rate of 1°–2° per day, corresponding to a radiative flux divergence of about 150 W m^{-2}. This cooling is largely balanced by a comparable surface flux, primarily of water vapor. As a result, precipitating deep convection is an inevitable element of the tropical atmospheric climate, linking the latent energy input at the surface with the radiative energy loss aloft.

Deep convection exhibits more large-scale[1] space and time variability than either radiative cooling or evaporation, as reflected for example in hourly or daily time series (Lin and Johnson 1996a,b). Large-scale circulations are necessarily involved, with one major component being a deep vertical overturning that redistributes the localized deep latent heating, keeping temperature nearly constant everywhere. Convective variability occurs on many space and timescales, each of which may offer clues about the relationship between deep convection and large-scale circulations. This relationship is important for tropical and global variability on all time-

---

Corresponding author address: Dr. Brian E. Mapes, NOAA–CIRES Climate Diagnostics Center, 325 Broadway R/E/CDI, Boulder, CO 80303-3328.
E-mail: bem@cdc.noaa.gov

---

[1] "Large-scale" means scales resolved by a $\sim$400-km grid and a $\sim$2-h time step. Smaller scales are "subgrid-scale."

scales, including climate variability, but is probably best isolated by studying subseasonal weather or waves.

A comprehensive space–time spectral analysis of subseasonal tropical convection variability was recently performed by Wheeler and Kiladis (1999, hereafter WK99), considerably extending the results of Takayabu (1994). They examined multiyear global satellite records of outgoing longwave radiation (OLR) and found a generally red spectrum, augmented by enhanced variability lying along the dispersion curves for linear equatorial shallow-water waves, characterized by an equivalent depth of around 25 m (Kelvin or gravity wave speed 15–20 m s^{-1}). Most of this wave variability has planetary wavenumbers <10, and ~3–20-day periods—distinct from the 30–60-day intraseasonal oscillation, which has a lower frequency and speed, and apparently involves mechanisms other than linear atmospheric wave propagation. Although these waves are a small fraction of the total convective variability, their nearly linear propagation characteristics and well-defined structures provide a clear challenge for theories of large-scale convection variability to explain. This challenge motivates the present study.

There is also a large body of knowledge about convection that comes from decades of in situ study of convective cloud systems in physical space, using visual, radar, aircraft, and sounding observations. A satisfying model of large-scale waves that involve variations of ensembles of convective cloud systems should be consistent with robust observational facts about these systems.

The remainder of this rather lengthy introduction (section 1) reviews a general body of ideas and observations that are offered to motivate and justify the model. Many of these ideas will seem obvious to some readers and controversial to others, so it seems necessary to lay out the whole physical picture and modeling philosophy at length, before proceeding to the details of model formulation, in section 2.

a. Convective clouds in nature

Cumulus clouds are ubiquitous in the Tropics (Warren et al. 1988) and are of first-order importance in maintaining the temperature and moisture structure of the lowermost free troposphere. Raymond (1995) deduced the omnipresence of moist convection, from the fact that θ_e in the thin subcloud layer remains closely bounded over evaporating warm oceans, with surface fluxes being balanced by moist-convective eddy fluxes out of the top of the subcloud layer. In this picture, convective inhibition energy (CIN, discussed below) in the mean state is determined by the statistical intensity of the boundary layer turbulence (including mesoscale variability) that constitutes the roots of these cumuli. That is, surface fluxes tend to decrease CIN until enough moist convection is able to grow from these roots and establish a "boundary layer quasi-equilibrium" (Ray-

mond 1995). CIN is an important parameter in the present model, so it is important to recognize the reasons behind its existence. Note also that CIN in this discussion is a property of a large-scale average sounding, so that within a grid box with nonzero mean CIN, convective clouds may be viewed as small subregions where *local* CIN has been reduced to zero by conspiracies of subgrid-scale fluctuations.

Some cumuli produce showers—enough that shipborne weather radars over warm oceans report echoes 99% of the time (e.g., Houze and Cheng 1977; Rickenbach and Rutledge 1998). The isolated showers during otherwise dry periods presumably represent the upper tail of the distributions of thermodynamic and cumulus-triggering energy within a fair-weather boundary layer.

This omnipresent population of cumuli produces, in aggregate, light to moderate amounts of rain, implying a mild condensation heating of the lower troposphere. For example, Fig. 4 of DeMott and Rutledge (1998) indicates unceasing daily radar-observed rainfall for 3 months in a 240-km square area of the western Pacific during the Coupled Ocean–Atmosphere Response Experiment (COARE) field campaign, composed of an omnipresent middle-topped echo population, plus the much more abundant, but intermittent, rainfall from deep convective systems. The middle-topped cloud population exhibits mild temporal modulation, with increases during the deep-convective disturbed periods and decreases during undisturbed periods.

The great majority of rain in COARE (and likely globally) occurred in the form of large, contiguous mesoscale deep-convective systems that are much more intermittent on large scales than are the congestus showers. This organized deep convection is dominant in terms of precipitation, latent heating, and OLR but is inconvenient to explain in terms of theoretical cumulus dynamics. For example, if CIN is in equilibrium with a statistically ubiquitous population of small entraining cumuli, then how can it be a significant factor inhibiting deep-convective cells, which should presumably suffer less entrainment due to their larger size? Such cumulus-oriented reasoning has led to the almost universal neglect of inhibition and triggering effects in convective (sometimes called "cumulus") parameterization schemes for global models.

The answer may lie in the well-observed fact that deep convection does not consist simply of giant cumulus clouds, springing spontaneously from ordinary boundary layer turbulence. Rather, it is organized on the mesoscale, largely by the action of its own downdraft outflows. Rickenbach and Rutledge (1998) report that 80% of the rainfall within the range of the Massachusetts Institute of Technology radar during Tropical Ocean and Global Atmosphere (TOGA) COARE was associated with well-defined lines of convective cells at least 100 km in length. These mesoscale convective features had associated stratiform precipitation accounting

for one-third of their total rainfall. Houze (1997) presented a review and discussion of stratiform rain, an important inclusion in the present model.

A main mechanism of organization of these mesoscale convective systems is the ''gust front'' or outflow boundary: the edge of a pool of evaporatively chilled air at the surface, generated by downdrafts in a prior generation of deep convective cells. The most famous example of this is the 2D squall line, but mesoscale systems of more general structure also tend to have their convective cells in unsteady, complicated lines. Deep convective lines are commonly observed to sweep through regions containing a population of preexisting cumulus clouds. This fact suggests that there is an empirically important, if theoretically irritating, distinction between shallow convection and organized deep convection: a patch of atmosphere may be capable of supporting either one, but mesoscale deep convection is apparently distinct in requiring a special initiation process at low levels. Essentially all of the deep convective cells producing rain in COARE were associated with gust fronts from prior convection (e.g., Kingsmill and Houze 1999).

This inconvenient difference between shallow and deep convection is incorporated into the present model in the form of separate parameterizations for spontaneously forming cumulus showers and deep-convectively triggered deep convection. This two-part treatment renders the model more empirical, but less conceptually simple, than models that attempt to treat all moist convection the same (as cumulus plumes of different sizes, for example).

b. Convective processes in the model

The effects of shallow cumuli are implicitly subsumed into the basic state. Their ubiquitous effects (i.e., effects assumed to occur within every 400-km grid box) are represented in four ways. First, a climatological-mean basic-state value of large-scale CIN is specified (CIN_0). Second, a small ambient value of deep-convection triggering energy ($K_0 \ll CIN_0$) is present everywhere, representing a small population of spontaneously occurring convection, which can nucleate deep convective development when CIN is reduced, for example, by wave dynamics aloft. Third, a lower-tropospheric shallow-convective heating is assumed to counter much of the radiative cooling of the lower troposphere (discussed further in section 1e and appendix). Fourth, surface fluxes of equivalent potential temperature (θ_e), beyond those that cause ''recovery'' of the boundary layer after deep-convective disturbance, do not continue to increase boundary layer θ_e. Rather, they are assumed to converge throughout the whole lower troposphere, maintaining

the mean humidity, which is assumed constant (cf. Fig. 10b of Mapes and Zuidema 1996).[2]

Representation of deep convection in the model is based on the following set of observationally based notions.

- Deep convective clouds involve free buoyant ascent and therefore depend on convective available potential energy (CAPE).
- High-θ_e air in the subcloud layer is a key factor for convection, even though net inflow is deep.
- Deep convection depends on subgrid-scale ''triggering energy,'' to overcome mean CIN.
- Convective system downdrafts decrease area mean θ_e, disfavoring new convection.
- These downdrafts also increase θ_e variance, such that some high-θ_e air remains in the area.
- Deep convection generates triggering energy (gust fronts, gravity waves, ''organization'').
- Deep convection spawns stratiform precipitation, which cools the lower troposphere by evaporation.

c. Thermodynamics and kinetics of deep convection

Observations of the bulk thermodynamics of deep convective regions of the Tropics are consistent with these observations of cloud system structure. Near-surface air has a modest negative buoyancy if lifted into the lowermost troposphere, below its level of free convection (LFC). The work done to lift air through this layer of negative buoyancy is called the CIN. Above the LFC, the air experiences positive buoyancy. The work done by this positive buoyancy (CAPE) drives circulations of a wide range of space and timescales. When precipitation is evaporated into lower-tropospheric air, the air can become negatively buoyant and descend. This thermodynamic process is active in convective system downdrafts. Downdraft air arrives at the surface with a low value of equivalent potential temperature θ_e, making it unfavorable for reascending (large CIN, small CAPE), but also with a high density, which can drive upward motion at narrow, intense gust fronts at airmass edge.[3] This upward motion can perform the work to overcome CIN, initiating further deep convection.

---

[2] In the present paper, to isolate thermal wave dynamics, humidity variations are neglected. In a ''prognostic humidity'' version of the model, column-integrated humidity is allowed to vary, with assumed vertical structure based on composite COARE sounding humidity variations. In that case, lower-precipitation-efficiency convection moistens the dry air at the leading edge of waves of rainfall, as in Raymond and Torres (1998). Qualitatively, though, the wave dynamics are the same as those presented here.

[3] A subtlety here is that the gust-front air, produced by convective-scale downdrafts, is cold but not very dry or low in θ_e (e.g., Addis et al. 1984). The decrease in θ_e is due largely to mesoscale downdrafts, where warm dry downward-displaced air is entrained down into the thin subcloud layer (Zipser 1977).

The exact values of CAPE, CIN, LFC, etc. in a given sounding depend upon debatable cumulus-dynamics assumptions about parcel definition, mixing, and thermodynamic and microphysical processes. Precise definitions of triggering energy and CIN that are quantitatively relevant to organized deep-convective cloud systems are unknown. CIN as used in this paper is simply an index, defined as the vertical integral of the negative part of the buoyancy profile of a grid-box mean subcloud-layer air parcel, with no mixing and simple specified microphysical processes. Triggering energy (K) in this paper is an index, in energy units (J kg^{-1}, like CIN), of all subgrid-scale low-level variability as it relates to deep convective initiation. It therefore covers subcloud-layer θ_e variability, gravity waves, and mesoscale organization (i.e., special or nonrandom spatial relationships), as well as gust-front vertical kinetic energy density (see section 3b). Although the absolute values of CIN and K are hard to validate with observations, they always appear in ratio. It is hoped merely that the CIN so defined will have relevant sensitivities to changes in boundary layer θ_e and to dynamically induced temperature changes aloft.

The present model illustrates the different large-scale dynamics that result from different assumptions about the sensitivity of deep convection to environmental conditions. These assumptions are built into simple source–sink equations with adjustable parameters defining the relative importance of various mechanisms, conceptually based on the cloud system structure and thermodynamic observations considered above. The general philosophy of this model is to consider perturbations around a climate state defined by observations, primarily from the 1992–93 TOGA COARE field program (e.g., Godfrey et al. 1998 and references). This is therefore a model of a ''warm-pool world'' in which the whole model domain has properties like the western Pacific warm-pool region.

d. A closed-system model of the Tropics

Because the export of latent and sensible heat from the Tropics to higher latitudes is only ~20 W m^{-2} (Fig. 13.12 of Peixoto and Oort 1992), a small fraction of the ~140 W m^{-2} radiative cooling and surface fluxes, it is a useful approximation to consider the Tropics as a closed system. A further simplification is to postpone inclusion of spatial inhomogeneities such as land areas and those regions of the tropical oceans where ocean dynamics maintain cold sea surface temperatures (section 5a describes a first attempt at including these as space-dependent terms in the θ_e and K equations). Additionally, it is convenient to initially reduce the system to one horizontal dimension, without rotation effects (section 5b includes a first attempt at extending these dynamics to an equatorial beta plane). Finally, all the cases in this paper assume that radiative cooling and surface flux are spatially uniform, to isolate convection

and wave dynamics from any cloud–radiative and evaporation–wind feedbacks.

Thermodynamic relationships and sensitivities are linearized about a COARE mean reference sounding. The model is designed to have as few variables as possible, but with sufficiently well-defined quantities that observations can be consulted where model parameters are needed. Empirical relationships are used to gain maximal realism within the simplest framework. This could be called a semiempirical toy model, in the spirit of simple tropical models by Raymond (1994), Chao and Lin (1994), Yano et al. (1995), Numaguti and Hayashi (1998), and Raymond and Torres (1998).

e. Convective heating profiles

The net radiative cooling of the model troposphere is 140 W m^{-2}. This number is chosen to resemble a climatological cooling of the tropical troposphere (Fig. 1). Deep convection and its variations are the main subject of this model, but deep convective heating has a top-heavy profile that does not balance the totality of radiative cooling. A ubiquitous shallow-convective heating (consisting of condensation plus vertical eddy heat flux convergence) is implied by the mismatch between profiles of radiative cooling and net heating in regions of concentrated deep convection (Fig. 1, see appendix for derivation and more discussion).

The mismatch between radiative cooling and deep convective heating profiles was ascribed by Gray (1973) to ''partly cloudy'' areas, derived as a residual from budgets of ''clear air'' (with no cloud processes by assumption) and deep-convective ''cloud cluster'' areas. In the present model, the concept of large-scale clear-air regions is not invoked; shallow-convective processes are envisioned to operate everywhere, albeit with some wave modulation.

In the subcloud layer, convergence of the dry turbulent sensible heat flux balances radiative cooling (e.g., LeMone 1995 and references; LeMone and Meitin 1984). At higher altitudes, turbulent heat flux convergence in shallow-cumulus cells may still play a role, but balancing the heat budget requires reference to a population of precipitating cumulus congestus clouds, with their tops in the midtroposphere, that are not as concentrated in space and time as deep convection. The widespread existence of such shallow, but precipitating, cumulus clouds has recently been reviewed and highlighted by Johnson et al. (1999). Figure 4 of DeMott and Rutledge (1998) shows that radar echoes (that is, precipitating clouds) with midlevel tops were present every day during COARE but were enhanced coincident with the deeper echoes that produce most of the rainfall. A similar impression of a ubiquitous population of congestus showers, punctuated by episodes of deeper organized convection with stratiform precipitation, was left upon the author during a recent cruise to the eastern Pacific ITCZ.
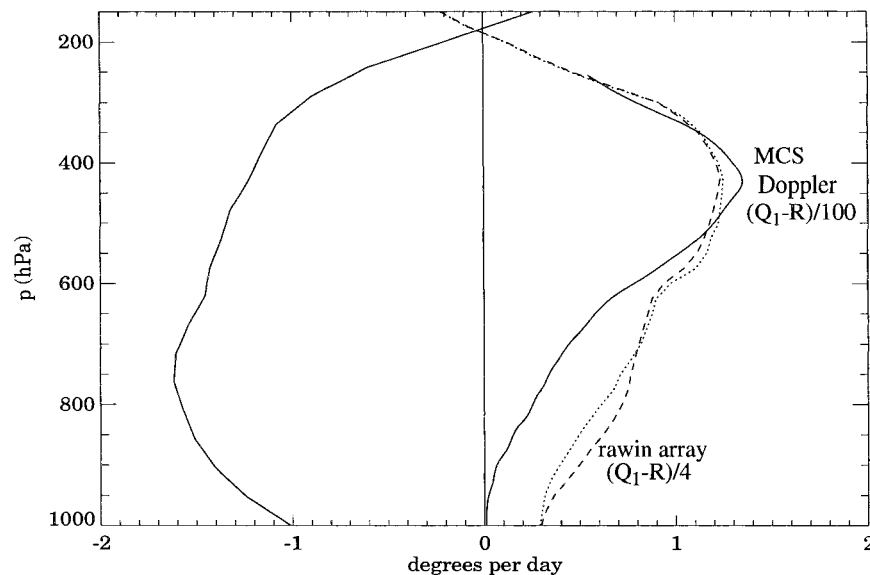
FIG. 1. Tropical average radiative cooling [negative values, computed by Bergman and Hendon (1998)], and deep-convective heating profiles (positive values, based on dry static energy export measurements at the perimeter of space–time regions in which deep convective activity is concentrated). The residual implies shallow-convective heating outside regions of concentrated deep convection. Broken lines are profiles of 120-day mean apparent heat source (Q_1), minus convective-region radiative cooling estimates from Bergman and Hendon (1998), scaled by 0.25. Dotted line: intensive flux array, dashed line: outer sounding array of the COARE field program. The solid line is a Q_1 profile based on the Mapes and Houze (1995) analysis of airborne Doppler radar data inside COARE mesoscale convective systems, scaled by 0.01. See appendix for details.

In the model, shallow-convective heating is assumed to be so ubiquitous that the imposed radiative cooling profile is simply corrected for its effects. Specifically, the model is subject to a total cooling profile that is the negative of the heating profile shown by a solid line in the right half of Fig. 1. Mapes and Houze (1995, hereafter MH95) showed that this profile consists, to a remarkable degree, of just two vertical modes of the dry
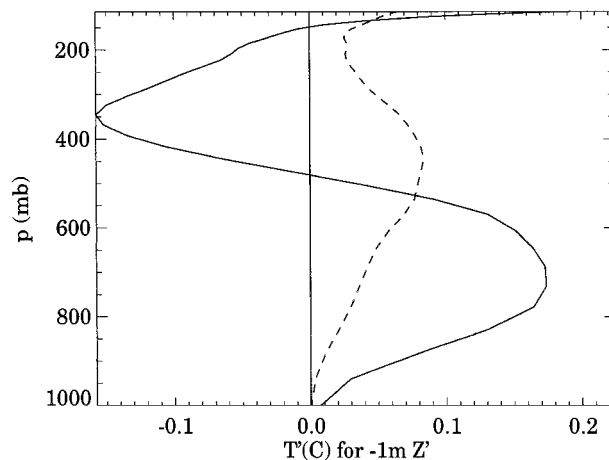

FIG. 2. Temperature structures of the two vertical modes carried in this model. From the Fulton and Schubert (1985) vertical transform, with a COARE mean virtual temperature sounding and a fixed top at 75 mb.

wave dynamics supported by the COARE observed tropospheric stratification. This is the basis for the two-mode truncation of vertical structure in Mapes (1998) and in the present study.

2. The model equations

a. The model dynamical core

The dynamics in this model are truncated to the first two internal vertical normal modes of the linearized primitive equations for perturbations in a realistically stratified tropical troposphere with resting basic state. These mode structures are defined by the Fulton and Schubert (1985) vertical transform, with a fixed top boundary condition at 75 mb. The temperature structures of the two modes are shown in Fig. 2.

The two modes will sometimes be referred to as the first and second tropospheric internal modes, or as "convective" and "stratiform" modes, after the parts of the deep-convective process that primarily excite them (see, e.g., Houze 1997). The convective mode, or first internal mode, is characterized by opposite-signed wind and geopotential in the lower and upper troposphere, with vertical velocity and temperature maximizing in the midtroposphere (dashed line in Fig. 2). Dry gravity or Kelvin waves with this first internal mode structure have a wave speed of $c = 52$ m s^{-1} (equivalent depth $c^2 g^{-1} = 275$ m). The stratiform or second mode is charac-

terized by a three-layer structure in the wind and geopotential fields, and two-layer structure in temperature (solid line in Fig. 2) and vertical velocity; it has a gravity wave speed of 23 m s^{-1} (equivalent depth 54 m).

Linear equations, governing the wind and geopotential height amplitudes for each of these two modes, compose the dynamical core of the present model, which may be solved in either one or two horizontal dimensions:

$$\frac{\partial \mathbf{u}_i}{\partial t} = -g\boldsymbol{\nabla}Z_i \qquad (1)$$

$$g\frac{\partial Z_i}{\partial t} = -c_i^2(\boldsymbol{\nabla} \cdot \mathbf{u}_i + D_i), \qquad (2)$$

where $\mathbf{u}$ denotes the horizontal wind; Z is geopotential height; $i = [23, 52]$ is a mode index, labeled according to gravity wave speed $c_i = [23, 52]$ m s^{-1}; and g is gravity. No rotation effects are included initially, but a Coriolis term will be added to (1) for the solutions of section 5b. The terms D_i are the radiative, convective, and stratiform heating rates, which appear as "diabatic divergence" (MH95), or mass-source terms in the shallow-water equations (1)–(2) resulting from the vertically transformed primitive equations (Fulton and Schubert 1985). The sign convention for both modes is that Z (free-surface height in the shallow-water analogy) represents low-level geopotential height. That is, $Z_i < 0$ implies warm air just above the surface, as might be generated by positive low-level heating $D_i > 0$.

The diabatic processes can be divided into radiative and convective parts, which balance in domain and time averages (climate balance) but not locally. The total cooling (sum of radiative cooling and ubiquitous shallow-convective heating, section 1e) is specified uniformly everywhere: Z_{52} is subject to a source of 17 m day^{-1}, while Z_{23} has a sink of 1.7 m day^{-1}. This corresponds to 80 W m^{-2} of net cooling, with the profile shown in the solid line in Fig. 1.

The rest of the model equations constitute a system for specifying the diabatic heating rates associated with convection.

b. The convective heating parameterizations

1) DEEP CONVECTION HEATING: THE CONVECTIVE MODE

Convective heating is equal to the cross-isentrope mass flux, which may be converted to a vertical mass flux with division by the static stability profile (constant in this model). The present scheme is based on the idea that the convective vertical mass flux in a grid box is proportional to the fractional area covered by convection times the vertical velocity in that convection. Here, the convective cloud development time is neglected; in essence, the convection is assumed to span the whole troposphere in 1 time step (~1 h).

The fractional area covered by convection is assumed to depend on the fraction of air parcels at low levels that can overcome the CIN and begin the free buoyant ascent process. This fraction depends on the CIN of the grid-box mean sounding, and on the amount of deep-convection initiation–relevant subgrid-scale variability within a grid box (as represented in the triggering energy variable K). The vertical velocity in convection is assumed to scale as CAPE$^{1/2}$, based on the idea that CAPE is converted to vertical kinetic energy in convective clouds.

Finally, a dependence on moisture availability is formally acknowledged, through a factor $f(q)$. In the present paper, this humidity dependence is disabled, $f(q) = 1$. Specifically, the convective-mode heating rate at each point is expressed in ratio to the radiative cooling $D_{52\mathrm{rad}}$:

$$D_{52c} = (-M)\exp\left(-\frac{\mathrm{CIN}}{K}\right)\sqrt{\frac{\mathrm{CAPE}}{\mathrm{CAPE}_0}}f(q)D_{52\mathrm{rad}}. \qquad (3)$$

The negative sign indicates that convective heating is opposite in sign to radiative cooling, while $M > 0$ is a normalization constant that sets the climatological mean. The exponential factor in (3) is a function with values between 0 and 1 (since CIN and K are defined to be positive only). When CIN/K is large, it asymptotes to zero, and when CIN/K is small it asymptotes to unity. It is a smooth version of the "throttle function" of Raymond (1994).

The exponential factor in (3) is called the Boltzmann factor in statistical mechanics. It is an integral of the upper tail of the Boltzmann distribution (from CIN to infinity). The Boltzmann distribution is the distribution of energy among ensembles of identical interacting subsystems in equilibrium. In molecular statistical mechanics, the parameter of the Boltzmann distribution [K in (3)] is the absolute temperature, converted to energy units by Boltzmann's constant. Hence K could, by analogy, be called the "temperature" of subgrid-scale variability: a single number that characterizes the whole distribution of subgrid-scale triggering energy (subgrid-scale variability as it relates to deep convective initiation). The assumption is that this subgrid-scale triggering energy resides in an ensemble of identical subsystems, exchanging energy so quickly that they are always in a state of statistical equilibrium.

The proportionality factor M in (3) is chosen such that in radiative–convective equilibrium, the thermodynamic climate of the model is given by the mean COARE sounding [see (12) in section 4]. The CAPE factor in (3) has a climate average near unity, while the humidity dependence $f(q) = 1$ in this paper.

2) DEEP CONVECTION HEATING: THE STRATIFORM MODE

Stratiform heating is parameterized as a heating process in the second internal mode of the troposphere that

lags the convective-mode heating, and decays exponentially, with a timescale T_{meso} (set to 3 h in this paper). Specifically,

$$\frac{\partial D_{23s}}{\partial t} = (-s)\frac{D_{52c}}{T_{meso}} - \frac{D_{23s}}{T_{meso}}, \qquad (4)$$

where s is the "stratiform fraction," 0.5 here, based on the divergence-profile observations of MH95. The sign convention (section 2a) is such that $D_{23s} < 0$ (opposite in sign to D_{52c}) in convection, based on the signs of the heating profile contributions at low levels. Other values of s affect the rate of growth of the "stratiform instability" modes, but not their phase speed or scale or the equilibrium amplitude. Timescale T_{meso} sets an upper limit on the frequency of unstable waves, since the positive correlation of D_{23s} and $-Z_{23}$ (heating and temperature) requires that positive values of Z_{23} that enhance convection still be present $\sim$3 h later, when the associated stratiform heating process peaks. The radiative cooling in the stratiform mode is also s times that in the convective mode, so thermal forcings by radiation and convection balance within each mode, in domain and time averages.

3) CUMULUS CONGESTUS MODULATION BY Z_{23}

Variations in the "ubiquitous" heating by cumulus clouds in the basic state are parameterized as a simple linear damping on Z_{23}, based on the idea that anomalous lower-tropospheric heating excites mainly the second internal mode. In reality it would excite both modes considered here, and other vertical modes as well, but its importance lies in its effect on the second mode. This damping is chosen to equal the radiative value of D_{23} when $Z_{23max} = 5$ m, in order to keep the standard deviation of Z_{23} near observed levels ($\sim$5 m; Fig. 13 of Mapes 1998). Since Z_{23} has a climatological mean near 0 by design, D_{23c} does as well:

$$D_{23c} = D_{23rad}\left(\frac{Z_{23}}{Z_{23max}}\right). \qquad (5)$$

When $Z_{23} < 0$, the lower-tropospheric temperature is anomalously warm (as in Fig. 2, solid line), reducing the buoyancy of any given air parcel in that layer. A resulting reduction in the "basic-state" shallow-convective heating of the lower troposphere is obtained by addition of a negative heating anomaly ($D_{23c} > 0$). This mechanism prevents the growth of Z_{23} anomalies beyond observed limits (Z_{23max}) due to stratiform instability (section 4a). Without (5), Z_{23} variations grow to ever larger values, and the CIN and CAPE linearizations (6) and (7) produce regions of large values adjacent to values truncated to 0. The resulting sharp edges excite $2\Delta x$ waves in the dynamic equations, and the solution gets noisy. The D_{23c} from (5) is added to D_{23s} from (4) and D_{23rad} to construct the total D_{23} in (2).
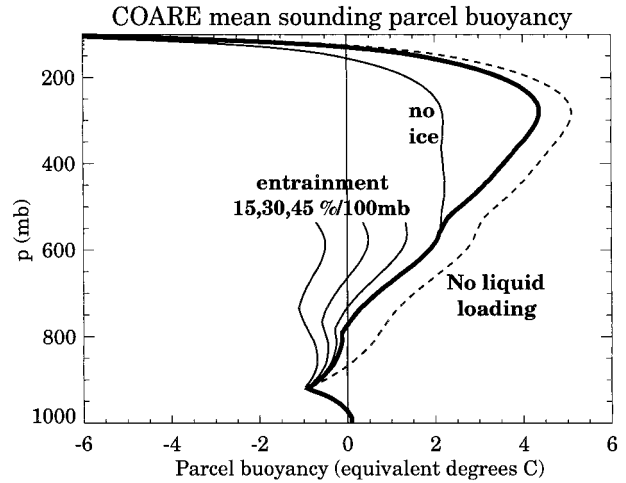

FIG. 3. Buoyancy profiles for a lifted parcel of mixed air from the lowest 50 mb in a COARE mean sounding. Heavy line is for undilute ascent with condensed water content truncated at 3 g kg^{-1}, representing precipitation processes, and latent heat of sublimatation added for water condensed above the 0°C (550 hPa) level. Light line above this level is without sublimation. Light lines below are for continuously entraining parcels with mixing rates of (from right to left) 15%, 30%, 45 % of parcel mass per 100-mb ascent. Dashed line is for pseudoadiabatic ascent (no condensate loading allowed).

c. CAPE, CIN, and their sensitivities

Equation (3) requires CAPE and CIN values at every model column. The model thermodynamics are linearized about a mean sounding from the TOGA COARE experiment. Parcel buoyancy profiles within this sounding are shown in Fig. 3, for various choices of thermodynamic, microphysical, and mixing assumptions. Absolute values of CAPE and CIN (the vertical integral of the positive and low-level negative parts of the buoyancy profile, respectively; both assigned a positive sign by convention) depend on assumptions but are normalized out by the choice of M in (3). Since we merely want CAPE and CIN indices that have the right sort of dependences on boundary layer θ_e, Z_{52}, and Z_{23}, we avoid complex specifications by taking CAPE and CIN from very simple calculations: a well-mixed parcel from the 1000–950-mb layer ascends with no entrainment, no ice processes, and precipitation processes assumed to truncate liquid water loading at a maximum of 3 g kg^{-1}. For these values, the mean sounding has a reference convective inhibition (CIN$_0$) of 23 J kg^{-1}, and a CAPE$_0$ of 800 J kg^{-1}.

The sensitivities of this mean sounding to boundary layer θ_e perturbations and to Z_{52} and Z_{23} (vertical displacements in the convective and stratiform vertical modes) were linearized, with coefficients determined by altering the sounding accordingly and recalculating the CAPE and CIN:

$$\text{CAPE} = \text{CAPE}_0 - aZ_{23} + bZ_{52} + c(\theta_e' - \theta_e^{eq}) \qquad (6)$$

$$\text{CIN} = \text{CIN}_0 - dZ_{23} - eZ_{52} - f(\theta_e' - \theta_e^{eq}), \qquad (7)$$

TABLE 1. Control parameters.

Parameter (equation)	Meaning	Value
$D_{52\text{rad}}$ (2)	Net cooling (radiation–shallow convection), 52 m s⁻¹ mode	-7.1×10^{-7} s⁻¹
$D_{23\text{rad}}$ (2)	Net cooling (radiation–shallow convection), 23 m s⁻¹ mode	3.6×10^{-7} s⁻¹
T_{meso} (4)	Stratiform evolution time	3 h
T_{BL} (9)	θ_e' damping (boundary layer recovery) time	4 h
T_{damp} (8)	K damping time	5 h
a (6)	$d(\text{CAPE})/dZ_{23}$	6 J kg⁻¹ m⁻¹
b (6)	$d(\text{CAPE})/dZ_{52}$	22 J kg⁻¹ m⁻¹
c (6)	$d(\text{CAPE})/d\theta_e$ at constant T_v	260 J kg⁻¹ K⁻¹
d (7)	$d(\text{CIN})/dZ_{23}$ for $Z_{23} > 0$	2 J kg⁻¹ m⁻¹
	for $Z_{23} < 0$	6 J kg⁻¹ m⁻¹
e (7)	$d(\text{CIN})/dZ_{52}$	0.6 J kg⁻¹ m⁻¹
f (7)	$d(\text{CIN})/d\theta_e$ at constant T_v	5 J kg⁻¹ K⁻¹
CAPE_0 (6)	Climatological CAPE	800 J kg⁻¹
CIN_0 (7)	Climatological CIN	23 J kg⁻¹
K_0 (8, 12)	Ubiquitous background K	3 J kg⁻¹
A_{cd} (9)	Convective downdraft θ_e depression rate	5 K/15 h/$D_{52\text{rad}}$
A_{sd} (9)	Stratiform downdraft θ_e depression rate	5 K/15 h/$D_{23\text{rad}}$
A_{cK} (8)	Convective K generation rate	-5 J kg⁻¹/3 h/$D_{52\text{rad}}$
s (4)	Stratiform D fraction ($-D_{23\text{rad}}/D_{52\text{rad}}$)	0.5
$Z_{23\text{max}}$ (5)	Z_{23} at which congestus heating D_{23c} equals $D_{23\text{rad}}$	5 m
K_{eq} (10)	Time average solution to (8)	8.3 J kg⁻¹
M (3, 12)	Maximum (uninhibited) D_{52c} at CAPE_0	7.6
θ_e^{eq} (6, 7)	Convectively induced θ_e' scale value	2 K

where θ_e' is the (negative-definite) convectively induced θ_e perturbation, and θ_e^{eq} is its climatic mean [steady-state solution to (9) below]. All six coefficients (a–f) are positive, with values in Table 1. A linear treatment was inadequate for the change of CIN with Z_{23} variations of ± 5 m amplitude, so a bilinear fit was used (two values for coefficient d; see Table 1). Boundary layer θ_e change was performed at constant virtual temperature. Both specific humidity and entropy were advected by the vertical displacements Z_{52} and Z_{23}; the temperature change (Fig. 2) was the dominant effect. Negative values of either CAPE or CIN from (6) and (7) are set to zero.

The formulation of the last term in each equation ensures that the model's mean sounding is the COARE mean sounding, even when the parameters controlling the mean convectively induced θ_e perturbation are changed.

The absolute value CIN in the COARE mean sounding is sensitive to humidity errors in the lowest levels of the COARE soundings. Recall that in this model, CIN always appears in ratio to K, the subgrid-scale triggering energy. While absolute values of both are subject to considerable observational and definitional uncertainties, the model really only relies on the physically well-founded assumption that CIN and K are comparable in convecting regions.

d. K and θ_e in the planetary boundary layer

The model equation for the subgrid-scale triggering energy variable $K = K_0 + K'$ contains a background term K_0 and a convectively generated part K', which obeys

$$\frac{\partial}{\partial t} K' = A_{cK} D_{52c} - \frac{K'}{T_{\text{damp}}}. \qquad (8)$$

In this equation, convective-mode heating processes ($D_{52c} > 0$) are assumed to be accompanied by a proportional source of K' (A_{cK}, the coefficient of the convective source of K, is positive). The K' also undergoes a damping with timescale T_{damp} (here 5 h). The processes by which convection generates K include surface gust-front generation by cold downdraft outflows, generation of variance of θ_e about its grid-box mean value, and the excitation of gravity waves (density fluctuations) in the layer in which parcels are negatively buoyant. The damping of K represents surface fluxes and vertical gravity wave propagation.

The model equation for θ_e is also a simple balance between convective forcing and a linear damping term:

$$\frac{\partial}{\partial t} \theta_e' = -A_{\text{cd}} D_{52c} + A_{\text{sd}} D_{23s} - \frac{\theta_e'}{T_{\text{BL}}}. \qquad (9)$$

Both the convective and stratiform downdraft coefficients (A_{cd} and A_{sd}) are positive, such that both convective ($D_{52c} > 0$) and stratiform ($D_{23s} < 0$ in convection) processes act to decrease θ_e, which is always negative. The linear restoration term, representing anomalous surface flux convergence that acts to restore the boundary layer toward COARE mean conditions, is characterized by a boundary layer recovery timescale T_{BL}, here taken to be 4 h.

The ratio of T_{damp} to T_{BL} is important to the character of the model solutions (section 4a), but the specific value of either one is not, within fairly wide limits (2–18 h). Since both time constants represent the action of surface fluxes in the boundary layer, they are given comparable values. No wind speed dependence of the surface fluxes is considered in this paper.

3. Observations behind model parameter choices

This section gives background information related to the values chosen for parameters in the control run (listed in Table 1). Section 4 explores model sensitivities to parameters in, and beyond, the observed ranges.

a. Boundary layer θ_e and recovery surface fluxes

Based on the observations of Kingsmill and Houze (1999), Young et al. (1995), and Addis et al. (1984), convective outflow air has θ_e depressions of a few to several degrees, while wake-recovery flux enhancements are roughly 20 W m⁻² per degree θ_e, implying a 7-h recovery time if the enhanced flux converges in a

50-mb layer. Since convective outflow air covers only a fraction of disturbed areas, θ_e^{eq} [the steady solution to Eq. (9)] is chosen to be -2 K. This choice constrains A_{cd} and A_{sd}, given T_{BL}, according to (9), and so sets the range for large-scale convectively generated variability in θ_e.

b. Observations and triggering energy K

In a similar manner, we need to choose a climate average (and therefore perturbation range) K_{eq}, as the steady-state solution to (8), which will define A_{cK} given T_{damp}. Observationally, the way to proceed is to seek a ratio of K to θ_e anomalies characterizing deep convective conditions, using aircraft, surface, and radiosonde data.

The energy K is a blanket representation of subgrid-scale variability, *as it relates to deep-convective system initiation.* As such, K would seem to have four main parts: gust-front vigor; fluctuations of θ_e about its grid-box mean value; density fluctuations in the lower-tropospheric inhibition layer; and organization, in the sense of special, favorable spatial relationships among these subgrid-scale variations. Humidity variability aloft is probably also a major factor, as convective clouds preferentially grow in the humidified wake of prior clouds. For the present discussion, which utilizes a non-entraining CIN as the index of inhibition, we ignore this large part of the problem, for tractability purposes only.

The first three are easily converted to K's energy density units (J kg^{-1}). Gust-front vigor may be expressed as vertical kinetic energy density. Variance of θ_e can be converted to CIN variance using coefficient f from (7). Density variations associated with lower-tropospheric gravity (buoyancy) waves constitute a fluctuation potential energy density (buoyancy integrated over height, like CIN) and can be estimated from radiosonde variances (e.g., Allen and Vincent 1995).

The fourth element of K—organization—is harder to quantify and involves the way in which the other three energy densities are assumed to combine to yield a value of K. For example, if subgrid-scale gust fronts, θ_e fluctuations, and gravity wave phase were uncorrelated, then K might be the root-mean-square of the three contributions, and hence not much bigger than any of them. On the other hand, if (as seems likely) gust fronts tend preferentially to lift high-θ_e air, perhaps through regions aloft that have been favorably preconditioned, then the total subgrid-scale triggering energy as it relates to deep-convective system initiation may be much larger than the root-mean-square.

This section briefly considers quantitative estimates for these effects. Numbers from the statistical studies of convectively disturbed boundary layers by Addis et al. (1984), Kingsmill and Houze (1999), and Young et al. (1995) are used to define typical values. This section is something of a digression, but the novelty of the formulation warrants some empirical discussion.
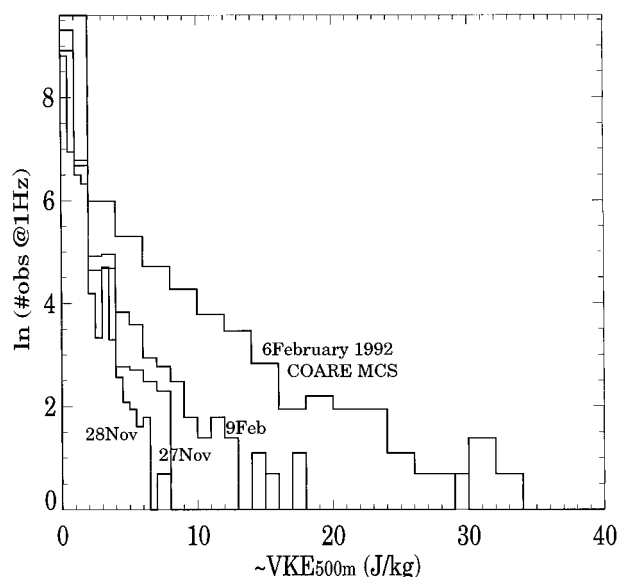

FIG. 4. Histograms of VKE $w^2/2$ for four COARE aircraft flights. The 1-Hz measurements of vertical velocity w between the surface and 1000-m altitude were adjusted to 500-m height, assuming linear increase with height. The number of VKE observations exceeding 5 J kg^{-1} corresponds with the degree of convective disturbance, from 28 Nov 1992 (undisturbed), to 27 Nov 1992, to 9 Feb 1993, to 6 Feb 1993, when a mesoscale convective band was sampled.

1) Vertical kinetic energy

Gust-front energy is estimated in two ways: the potential energy of a cold pool of convective outflow air, and the vertical kinetic energy sampled by aircraft. For a 3-K θ_e depression, a typical virtual temperature depression is $\sim 2°$. If this cold air is assumed to be 500 m thick, then the potential energy can be estimated as buoyancy times height, 33 J kg^{-1}. The appropriate area average of subgrid-scale gust-front energy is some fraction of this, depending on the perimeter-to-area ratio characterizing cold-pool geometry. A more direct estimate for vertical kinetic energy (VKE $= w^2/2$, where w is vertical velocity) at the top of the subcloud layer may be generated from aircraft data. Figure 4 shows histograms of VKE at subcloud-layer top from four flights, with differing levels of convective disturbance. Boundary layer data for w are adjusted to 500-m altitude by assuming linear variation with height. For the most disturbed flight on Fig. 4, the slope on this logarithmic plot is about 5 J kg^{-1}, implying a distribution of vertical kinetic energy $f(\text{VKE}) \sim \exp[-(\text{VKE})/5 \text{ J kg}^{-1}]$.

2) Subgrid-scale variability in θ_e

Kingsmill and Houze (1999) compiled histograms of θ_e from extensive aircraft sampling of the boundary layer in regions of inflow and precipitation associated with convection. Their Table 3 shows that the average difference between inflow and precipitation region θ_e was 3.1 K, while the standard deviation of θ_e was 1.9

K greater in the precipitating regions. Converting these differences to CIN units using f from (7), a 3.1-K decrease in mean θ_e (15.5 J kg^{-1} increase in mean CIN) is mitigated by a 1.9-K upward shift of θ_e (9 J kg^{-1} downward shift of CIN) for air 1 standard deviation above the mean. If convection draws selectively on this 1-sigma tail of the θ_e distribution, then a ratio of 9 J kg^{-1} per 3.1 K is implied for the K'/θ'_e ratio due to distribution broadening, alone.

3) GRAVITY WAVES IN THE INHIBITION LAYER

The gravity wave part of K can be estimated from climatological gravity wave energy density (Allen and Vincent 1995). Tropical convective-season energy densities are ~5 J kg^{-1} in northern Australia in the lower troposphere. This value can be approximately associated with the climatological deep-convective wake perturbation θ'_e of -2 K assumed here. A specific aircraft data example of a gravity wave in the lower troposphere near convection can be seen in Mapes (1997a). In that case, a 1°C temperature anomaly through 300-m depth suggests a ~10 J kg^{-1} inhibition change near a large convective system.

4) COMBINING THESE ESTIMATES TO MAKE A FINAL CHOICE

In summary, triggering energy generation by convective-system downdrafts has magnitudes about 5–10 J kg^{-1} for each of the three effects outlined, for typical θ_e depressions of 2–3 K. Here we select the ratio of 15 J kg^{-1} per -3 K for deep-convective generation rates of K' and θ'_e. There are also practical numerical considerations in the choice of parameters controlling K (section 4). We also choose similar damping times for K' and θ'_e (T_{damp} and T_{BL}, 5 and 4 h, respectively). The near-unity ratio of these damping times is far more important to the solutions than the absolute values.

4. Model regimes and their parameter dependence

The control set of parameters is summarized in Table 1. The regimes into which model dynamics fall can be more simply understood in terms of higher-level quantities that are combinations of the basic parameters. As section 3 illustrated, these derived quantities may be easier to estimate or observe than the individual coefficients appearing in the equations.

Two important derived parameters are the equilibrium (climate) values of K' and θ'_e:

$$K'_{\mathrm{eq}} = -T_{\mathrm{damp}} A_{cK} D_{52\mathrm{rad}} \tag{10}$$

$$\theta_e^{\mathrm{eq}} = T_{\mathrm{BL}}(A_{cd} D_{52\mathrm{rad}} - A_{sd} D_{23\mathrm{rad}}), \tag{11}$$

where the "rad" subscript indicates radiative cooling rates. A further important value is M, from (3):

$$M = \exp[\mathrm{CIN}_0/(K_0 + K'_{\mathrm{eq}})]. \tag{12}$$
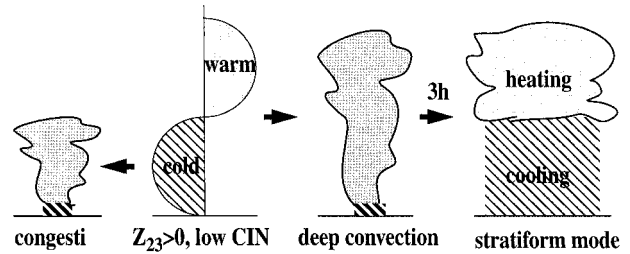

FIG. 5. Schematic illustrating the stratiform instability mechanism in the model. When Z_{23} has a positive perturbation, deep convection is enhanced through the exponential term in (3), leading with a 3-h delay to a stratiform heating process that is a positive tendency on Z_{23} (rightward arrows). At the same time, linearly increased heating of the lower troposphere by cumulus congestus showers [Eq. (5); leftward arrow] imparts a negative tendency on Z_{23}, capping the unstable growth of the Z_{23} waves at a finite amplitude (here 5 m, based on an observational upper limit).

The M determines how inhibited the convection is, on average, and hence how intense it can be where the inhibition is breached. Values of M greater than ~10 can lead to large gridpoint–to–gridpoint variability. Another important quantity is the ratio of T_{damp} and T_{BL}; their specific values are of secondary importance.

a. Model regimes with wide-ranging parameters

We now have a closed set of equations, with a stable radiative–convective equilibrium climate characterized by the COARE mean sounding. The equations are time stepped on a periodic one-dimensional grid of 100 grid boxes, 400 km in dimension, with no Coriolis force. Initial conditions include white noise in K (20% of K_{eq}), but all evolution is deterministic. Wind-induced surface flux enhancements are not operating in these runs.

Extensive experimentation reveals that the model outputs exhibit three main regimes:

1) CAPE controlled: When the "inhibition control" [the exponential term in (3)] is unimportant, as when CIN$_0$ is small, or K_0 or K'_{eq} is large, the model exhibits no variability; moist-convective damping (MCD; Emanuel et al. 1994) acts to diminish all waves. Convective heating preferentially occurs where CAPE is greatest, that is, where the temperature anomaly aloft is negative. The negative correlation between heating and temperature destroys wave energy.

2) Inhibition-controlled: When the inhibition control is the dominant source of variability in (3), an instability is possible. This stratiform instability depends on the fact that stratiform heating can have positive correlation with temperature perturbations in the second vertical mode (Fig. 5). For example, when Z_{23} is positive, the lower troposphere is anomalously cool. This implies decreased CIN, which enhances deep-convection frequency through (3), which leads, after a time delay of $T_{\mathrm{meso}} = 3$ h, to anomalous strat-
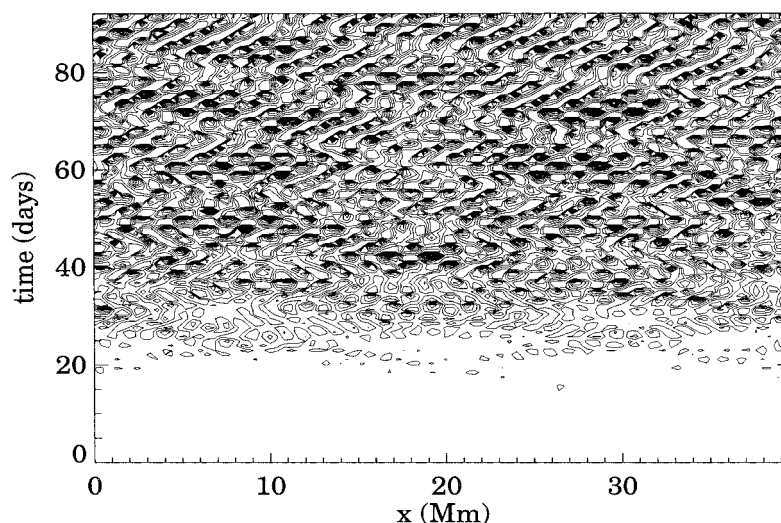
FIG. 6. Time–longitude section of convection ($D_{s_{2c}}$) in the shortwave subregime of the inhibition control regime, obtained when $\theta_e^{eq} = 4$ K. Convectively induced excursions of θ_e cause a local negative feedback and, hence, high-frequency oscillations with a period derived from the boundary layer recovery time. Contour interval $-0.4\ D_{52\text{rad}}$. Values near $-D_{52\text{rad}}$ on day 0 give rise to numerous small-scale regions of smaller and larger values.

iform heating in the upper troposphere and cooling in the lower troposphere—forcing that is in phase with the original Z_{23} anomaly. This instability can act to favor growth of waves of Z_{23} with any period that is long compared to T_{meso}, the time lag between convective initiation and stratiform heating corresponding to wavelengths longer than $(23\ \text{m s}^{-1}) \times T_{\text{meso}}$ or 2500 km. The actual wavelengths that occur depend on the relative importance of K and θ_e variations induced by convective-system downdrafts (discussed below). The growth of Z_{23} waves by stratiform instability is arrested by the assumed modulation of the basic-state cumulus heating D_{23c} [(5) in section 2b(3)], until the stratiform instability and "congestus damping" reach an equilibrium, with Z_{23} amplitude near the observationally determined target amplitude [$Z_{23\text{max}} = 5$ m in (5)].

3) Superinhibited: When CIN_0 is much greater than ($K_0 + K_{\text{eq}}$), so that $M > 10$ or so, the solutions take on a speckled appearance, with convection occurring intensely at some grid points and not at neighboring grid points. For marginal values of $M \sim 10$ this speckled pattern can appear and disappear within well-behaved larger-scale waves. Although numerically stable, and possibly physically relevant, this regime is not explored further here, as it depends upon the $2\Delta x$ computational mode of the discrete numerics.

Within regime 2, the inhibition-controlled regime exhibiting stratiform instability, there are two notable subregimes. The first occurs when the fluctuations of θ_e caused by convective-system downdrafts are more important to the convective variability than fluctuations of

K. In this case, downdrafts are a negative feedback on convection locally, and so convection tends to fluctuate with a period related to the boundary layer recovery time. Wave dynamics organize this oscillation into propagating waves with a corresponding short wavelength. Figure 6 shows an example of one such case, obtained by setting T_{BL} to 8 h instead of the control value of 4 h. In the second subregime, by contrast, when convection affects K more strongly than θ_e, a local positive feedback occurs, in which convection leads to more convection. In this case, long periods, and hence large wavelengths, are preferred (as in Fig. 7, obtained by setting $T_{\text{BL}} = 2$ h). The control run, with $T_{\text{BL}} = 4$ h, lies in between Figs. 6 and 7, with some tendency for high-wavenumber accents on the predominantly low-wavenumber waves (Fig. 11a).

Short wavelengths are also observed when the delay between convection and K' is shortened (A_{cK} doubled and T_{damp} halved; K'_{eq} remaining unchanged). In this case, convection flare-ups develop rapidly and then are limited and reversed by the negative feedback of θ_e depression, yielding fast oscillations with a frequency set by the boundary layer recovery time T_{BL}. The ratio $T_{\text{damp}}/T_{\text{BL}}$ is the important quantity here. These explanations summarize the results of extensive numerical experimentation but have not been analytically demonstrated.

b. Control run

1) COMPARISON TO OBSERVED WAVES

The model was run 35 times from different realizations of white initial noise, using the parameter values
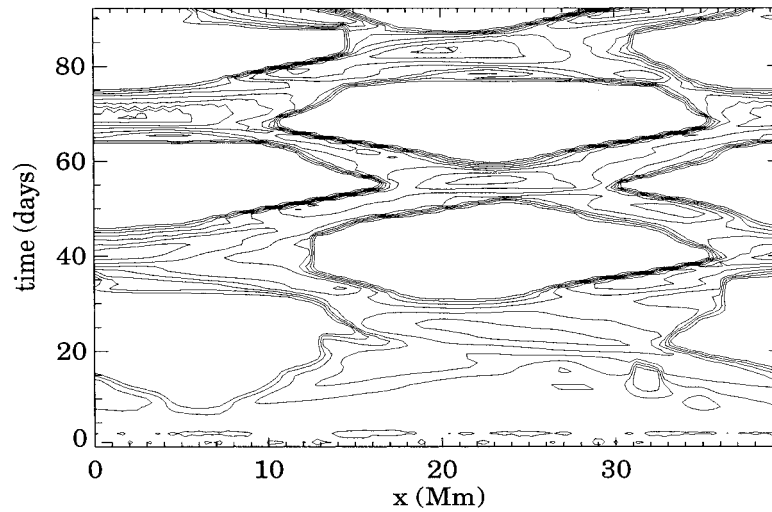
JOURNAL OF THE ATMOSPHERIC SCIENCES

VOLUME 57

FIG. 7. Time–longitude section of convection (D_{52c}) in the longwave subregime of the inhibition control regime, with $\theta_c^{eq} = 1$ K. Convectively induced excursions of K cause a local positive feedback and, hence, low-frequency oscillations favoring the lowest few spatial wavenumbers of the domain. Contours as in Fig. 6.

in Table 1. (An example run is shown in Fig. 11a.) Space–time spectra of model output have been computed, for comparison with the space–time spectra of OLR and MSU atmospheric layer temperatures by WK99. For this purpose, the D_{23} field has been chosen as a proxy for the OLR convection index used by WK99: it is negative in sign for positive convection anomalies, and it lags the convective-cell heating by $T_{meso} = 3$ h. Temperature indices corresponding to the MSU channel 2/3 (middle troposphere) and channel 3/4 (upper troposphere) temperature fields analyzed by WK99 are constructed, by reference to Fig. 2 and the vertical weighting functions of Spencer and Christy (1992):

$$MSU_{23} = -Z_{23} - Z_{52} \qquad (13)$$

$$MSU_{34} = Z_{23} - Z_{52}. \qquad (14)$$

After a 40-day spinup period, 95-day segments were analyzed, as in WK99. The results of this space–time spectral analysis, plotted to facilitate comparison with the eastward-symmetric part of Fig. 4d of WK99 (the Kelvin wave, whose propagation mechanism is like the nonrotating gravity wave here), are shown in Fig. 8.

Figure 8 indicates that the model's moist wave variability has speeds slightly slower than 23 m s^{-1}, as observed by WK99. The minimum in variability along the 52 m s^{-1} line, also present in observations, is presumably due to the damping effects of CAPE dependent heating on the deep temperature waves with 52 m s^{-1} speed. The 1/8–1/4 period lag of MSU$_{23}$ behind OLR in the main wave variance region (phase arrows in Fig. 8) agrees well with WK99's observations, as does the 1/4 wave MSU$_{34}$ lag behind OLR (not shown). Low-wavenumber, high-frequency oscillations with the opposite phase lag (wavenumber 1, ~4-day period; and

wavenumber 0, leftward-pointing arrows clipped from plot) are also present. In WK99, similar zonally symmetric and zonally extended oscillations with this phase relation are seen, but at lower frequency.

Figure 9a indicates the x–z temperature structure of model-generated eastward-propagating waves (selected by running the model with random initial conditions until an eastward-moving wave dominated the pattern). A reference time series of D_{23s} (OLR proxy) at the central longitude was correlated with Z_{52} and Z_{23} time series at other longitudes. The correlation coefficients were scaled by the corresponding standard deviations of Z_{52} and Z_{23} to yield regression values as a function of longitude. Each mode's regression structure was then multiplied by the temperature profiles of Fig. 2, and the two modes were superposed to yield the total wave structure. This procedure emulates the observational study by Wheeler et al. (2000), whose Kelvin wave temperature structure is shown in Fig. 9b for comparison.

The "boomerang" shape in Fig. 9a, with a cold anomaly behind (west of, in this case) the convection, wrapped around a midtropospheric warm anomaly ahead of the convection, resembles the observed structure (Fig. 9b), although the two-mode treatment of vertical structure distorts the picture. The second vertical mode is too prominent in the model. A similar tilted temperature structure characterizes the other tropical waves in Wheeler et al. (2000) and agrees with earlier literature (e.g., Nitta 1970). A recent study by Haertel and Johnson (1998, their Fig. 11) of westward-moving waves with a 2-day period showed similar temperature structure. In that study, reduction of CIN was cited as the key mechanism of propagation of convection anomalies.
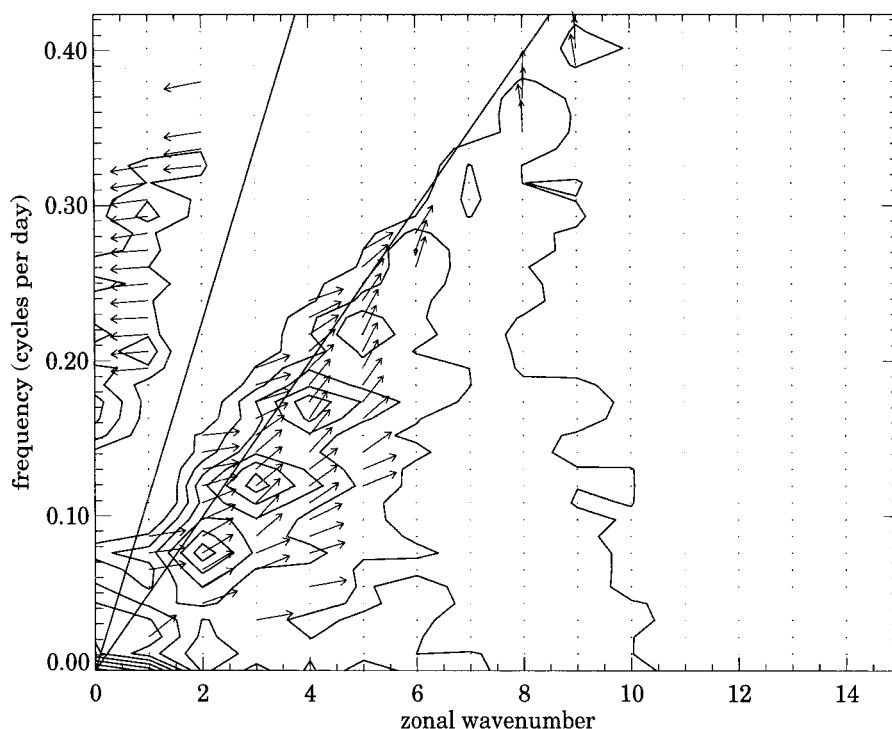
Unauthenticated | Downloaded 10/11/23 02:37 AM UTC

FIG. 8. Contours: logarithm of space–time spectral power density of D_{23s} in an ensemble of 50 96-day runs from random initial noise. Arrows: phase lag between D_{23s} and MSU_{23} (13), plotted only where D_{23s} spectral density and cross-spectral coherence are high. Arrows pointing to the right (left) of straight up indicate D_{23s} leading (lagging) MSU_{23}. Solid lines indicate 52 and 23 m s^{-1}, the two dry gravity wave speeds in the model. Comparable to Fig. 4 of WK99 for Kelvin waves, whose zonal propagation dynamics this nonrotating 2D model run best approximates. Zero-frequency peak comes from a fixed 1-K wavenumber-1 climatological-θ_e pattern, as in Fig. 12.

In the model, this tilted boomerang temperature structure is the sum of the one-signed convective-mode temperature structure, which is in horizontal and temporal quadrature with the convection, plus the two-signed stratiform-mode temperature structure in phase with the convection. To understand the model's wave dynamics, let us consider these phase relations in order.

The lag between D_{52} and Z_{52} is such that maximum deep-convective heating coincides with decreasing temperature. This indicates that adiabatic cooling more than counters the heating in the deep-convective vertical mode. Emanuel et al. (1994) showed that such a relationship characterizes a reduced-gravity moist Kelvin wave, in an atmosphere with a "statistical equilibrium" convection closure. In their picture, the propagating wave acts to cool the troposphere, and the convection responds rapidly[4] with countervailing condensation heating. This convective heating does not quite equal the adiabatic cooling, though, because in statistical equilibrium the tropospheric temperature remains linked by

a moist adiabat to the (area average) subcloud-layer θ_e, which is decreased by the convection's downdrafts.

In the present model, the dynamics in the deep-convective vertical mode are quite different. The speed of propagation of the moving convection is set by the second-internal-mode temperature wave (slowed slightly by moist processes, for unknown reasons), and not by the first internal mode feeling a reduced static stability due to moist processes. The relationship seen here (temperature decreasing during maximum heating rate) is simply the steady solution to a slowly moving heat source in a stratified fluid; it holds even if the heating (D_{52}) has no sensitivity whatsoever to deep-layer temperature (Z_{52}). To see this, consider the steady solution to (1)–(2), in a coordinate system moving with the heating: time derivatives are replaced with advection by the mean wind in the moving reference frame. The solution for imposed heating (D_{52}) with a sinusoidal form has minimum temperature lagging the heating by a quarter wavelength. Physically, the cold temperature (high surface pressure) behind the heating is necessary to cause the low-level wind to converge and ascend in the heated region. Evidently, the observed quadrature relationship between deep heating and temperature does not nec-

---

[4] Instantly, in strict statistical equilibrium, yielding a neutral wave; any delay causes wave decay by MCD (Emanuel et al. 1994).
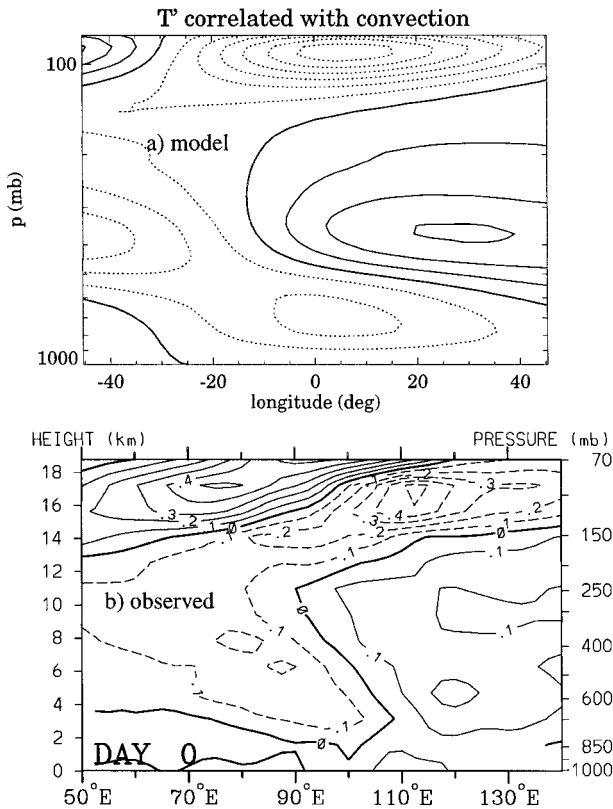
FIG. 9. Longitude–height sections of temperature regressed on a convection time series at a reference longitude. (a) Model result: regression coefficients are scaled so that the contour interval is 0.25°C for a 1-standard-deviation positive convection anomaly. Zero contour heavy, negative contours dotted. (b) Observational result, from Wheeler et al. 2000: OLR at 90°E, filtered for Kelvin wave variability only, was used as the reference convection time series, while temperature was taken from the National Centers for Environmental Prediction reanalyses. Contours: 0.1°C interval for a 1-standard-deviation OLR anomaly.
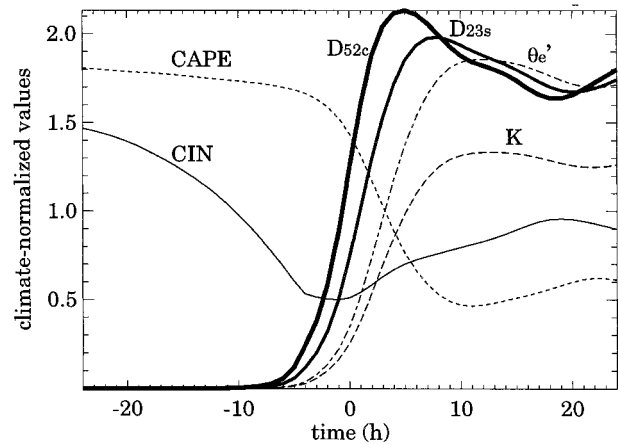

FIG. 10. Model variables, normalized by their climatological means, during a transition from dry to disturbed conditions (arrival of the rainy phase of a model wave).

essarily indicate the validity of a statistical-equilibrium convection closure.

In contrast, the stratiform temperature anomaly (Z_{23}) is in phase with the convection anomaly. In the model, this is because Z_{23} anomalies are a direct cause of convection anomalies, through reduction of CIN. The in-phase relationship of Z_{23} and convection, and the quadrature relationship of Z_{52} and convection, should persist in averages over any sort of larger-scale disturbances that contain stratiform-instability waves.

2) PHASE RELATIONSHIPS IN MODEL WAVES

Other phase relationships in the model are shown in Fig. 10, around the time of a flare-up of deep convection in a previously undisturbed grid box. Convective heating (D_{52c}) is lagged in succession by stratiform heating (D_{23s}, with delay time $T_{meso} = 3$ h), subgrid-scale variance (K, with delay $T_{damp} = 5$ h), and θ_e [with delay $T_{BL} = 4$ h, but responds to stratiform (D_{23s}), as well as

convective, downdrafts]. CAPE, which has built up to maximum values in the dry period, plunges with the development of the boundary layer θ_e depression. The variable that presages (and causes) the convection increase is CIN, which decreases in the hours before convection, owing to the arrival of a large-scale wave of lower-tropospheric cooling ($Z_{23} > 0$). CIN remains low (and Z_{23} remains high) as the convection continues.

3) REPARAMETERIZATION EXPERIMENTS

The temporal lags discussed above are so short that observations of the large-scale waves in the tropical atmosphere might not resolve them. To what extent can the processes governing large-scale convection variations be deduced from inexact observations? To address this question, approximate relationships, developed from perfect data about model variables, can be inserted in place of the model governing equations as "re-parameterizations." The subsequent evolution of the model fields then indicates whether these relationships capture the essential processes.

In this case, we know the form (3) of the relationship directly governing the convection variations. Since the variable triggering energy K is a novelty that we might wish to transplant to more sophisticated models, and since adding new a prognostic field to a big model is costly and difficult, could the K' equation (8) be replaced by a diagnostic equation?

The K' field is highly correlated with other convection-associated fields, because the lags between the fields (Fig. 10) are all small with respect to the timescale of the large-scale variations (Fig. 11a). In other words, a "quasi-equilibrium" prevails between K' and the other convection fields. What happens if we replace K at every time step with an appropriately rescaled copy of a field with which it is highly correlated diagnostically?

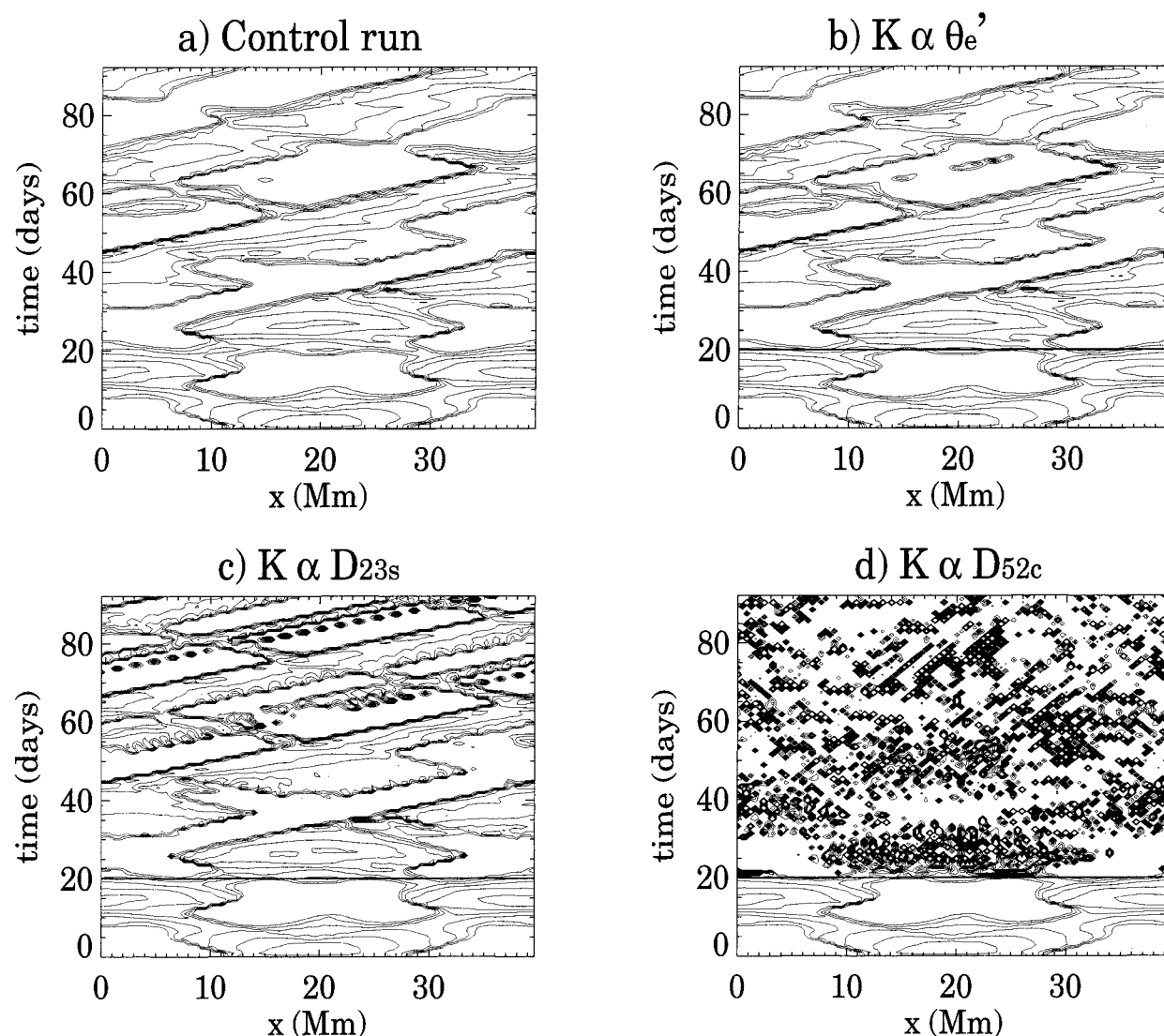Figure 11 shows the results of this experiment, with

a) Control run

b) K α θe'

c) K α D23s

d) K α D52c

FIG. 11. Time–longitude plots of convective heating (D_{52c}) in the last 95 days of 135-day runs, with Table 1 parameters and identical initial white noise. (a) Control run. In others, the K field is replaced at every time step, after plotted day 20, with appropriately rescaled patterns of other model variables. (b) θ_e (correlation in control run 0.9999), (c) D_{23s} (correlation in control run 0.9973), (d) D_{52c} (correlation in control run 0.9924). Small delay-time errors reflected in these slightly imperfect correlations shift the dynamics into entirely different regimes.

K patterns diagnosed at each time step from θ'_e (correlation -0.9999 in time step data from the control run), D_{23s} (correlation 0.9974), and D_{52c} (correlation 0.9923). Only in the first case do the waves continue with similar properties. Even a diagnostic relationship with >0.99 correlation in perfect observations does not necessarily constitute an adequate observational basis for a quasi-equilibrium parameterization of K.

The dynamics of these waves are sensitive to the slight time lags between the relevant variables. For example, in Fig. 11c, when K (with its 5-h lag behind D_{52}) is replaced by rescaled D_{23} (with a 3-h lag), higher-frequency waves develop. As discussed in section 4a, this regime results from the K positive feedback flaring

up too quickly, limited by the relatively slower dynamics of θ_e depression, yielding oscillations with a θ_e recovery timescale. The more extreme failure of the simulation in Fig. 11d is not simply a consequence of 0.9923 being too small a correlation. Rather, it arises because K and D_{52c} differ from each other by a systematic time lag. Note K is an instantaneous cause, but a delayed (accumulating) consequence, of D_{52c}. Figure 11d may be viewed as a strict or instantaneous statistical equilibrium parameterization, and the speckled or white noise appearance of the fields is consistent with Yano et al.'s (1998) findings on the behavior of such closures.

The success of a θ'_e parameterization of K is not entirely coincidental, as the same cold downdraft air that
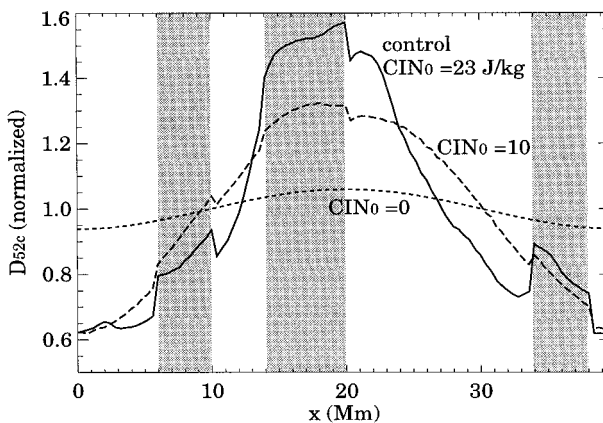
FIG. 12. 90-day-mean convective heating $(-D_{52c}/D_{52rad})$. A 1-K climatological wavenumber-1 θ_e perturbation maximum at $x = 20$ Mm is added when calculating CAPE and CIN, representing SST variation. Background subgrid-scale triggering energy K_0 is elevated from 3 J kg^{-1} to 4 J kg^{-1} in three shaded regions, representing continental and coastal triggering energy enhancements. Solid curve, control parameters; dashed curve, CIN$_0$ = 10 J kg^{-1}; dotted, CIN$_0$ = 0 J kg^{-1} everywhere (CAPE controlled regime).

reduces grid-box mean θ_e is also responsible for increasing θ_e variance, one of the effects represented by K. Since it is not trivial to introduce new prognostic fields in a full-blown GCM, a parameterization of K might be made in terms of recent downdraft activity as evidenced in gridpoint mean thermodynamic fields.

Emanuel (1993) also concluded that small convective-process time lags are of first-order importance to low-frequency wave dynamics. More discussion of lags and causality in tropical convection is in section 4 of Mapes (1997b). Pan and Randall (1998) introduced a ''prognostic closure'' formally identical to (8), although justified with different physical arguments, into the cumulus parameterization scheme of a GCM. They found that the model climate was quite sensitive to the choice of parameters determining the short ''adjustment time.''

5. Additional experiments and extensions

a. Climatology with an SST-like θ_e anomaly and continent-like K_0 anomalies

A time-independent wavenumber-1 θ_e perturbation with 1-K amplitude was added to the θ'_e from (9) before calculating CAPE and CIN in Eqs. (6) and (7). This may be thought of as a crude representation of sea surface temperature (SST) variability. In addition, the background triggering energy K_0 was elevated from 3 to 4 J kg^{-1} in three areas, roughly where the equatorial continents of the earth lie with respect to the Indo-Pacific warm pool.

Figure 12 shows climatological convection patterns in different model-dynamics regimes. In the CAPE controlled limit (dotted), in which triggering effects are unimportant, convection shows a small smooth variation

with longitude. The convection-induced θ'_e counteracts the imposed sinusoidal variation of θ_e, further flattening the already flat $[\text{CAPE}_0 + c (1 \text{ K}) \cos(\text{longitude})]^{1/2}$ curve that might be anticipated from (3) and (6). In a more inhibition-controlled regime (solid curve, control-run parameters), the sensitivity of convection to SST is considerably greater, and the convection-triggering effects of continents add distinctive features to the climatology. Wave effects also shape the climatology over the large ocean region from 20 to 34 Mm.

Of course, the specifics of this figure are model dependent. The general issue is that CIN and CAPE may vary *separately* with SST. Although these variations are invariably in the same sense (favoring convection over warmer water), they are not identical. Determining the regime parameters for real convection is therefore important to an understanding of climatological circulations, as well as of weather or wave variability. Given the difficulties with quantitative measurement of precipitation, it may be easier to recognize the gross differences between wave properties in the different regimes than it is to measure the differences between climatological rainfall curves like those in Fig. 12.

b. A β plane

It is possible to solve these equations in two horizontal dimensions, with the Coriolis force included. In this case, we choose a beta plane centered on the equator, with rigid walls at 72° latitude. When all parameters except the Coriolis force are uniform, Kelvin waves along the equator are preferred after a sufficiently long evolution from random initial conditions (Fig. 13). In this realization, a strong wavenumber-4 component is evident. The equatorial Kelvin waves are much like the waves in the 2D nonrotating case examined above, although they are eastward propagating only.

6. Discussion

A simple model of large-scale tropical convection waves has been constructed. When CAPE control dominates, all waves are damped by convection. When inhibition control dominates, large-scale waves are generated. The mechanism is here termed stratiform instability (Fig. 5), because it depends on two-signed tropospheric temperature waves, which are generated predominantly by two-signed heating in stratiform precipitation areas within deep convective systems (see, e.g., Houze 1997). This study points to high vertical wavenumbers to explain the slow ($\sim$20 m s^{-1} for Kelvin and gravity waves) propagation speeds of quasi-linear equatorial convection waves (as observed by WK99), rather than to the effects of moisture on the first internal mode of the troposphere (e.g., Yu et al. 1998).

The model is intended to encapsulate a view of convection derived from field experience of mesoscale convection observation. A prominent issue is the separate
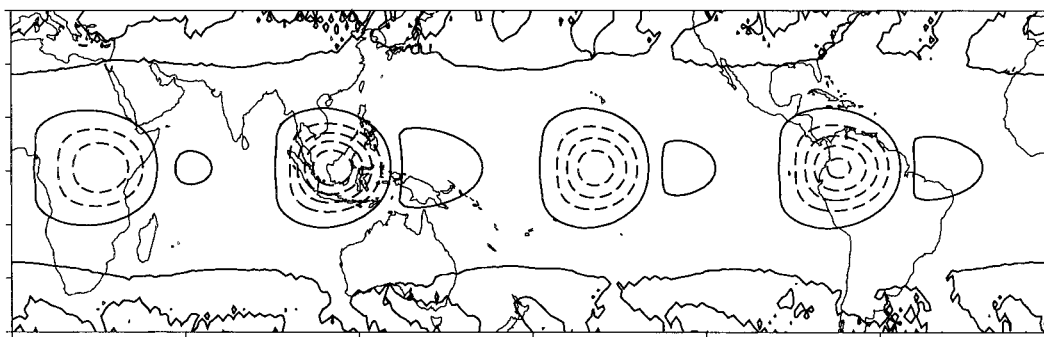
FIG. 13. Normalized convective heating ($-D_{52c}/D_{52rad}$) snapshot at day 84 from a model run with control parameters on an earth-sized periodic β-plane channel. Contour interval is 0.08 D_{52rad}, with regions of suppressed convection (values smaller than $-D_{52rad}$) dashed. Map overlay is for scale only.

treatments of shallow convection, which is nearly ubiquitous, and deep convection, which exhibits dramatic space–time variability.

A strong CIN dependence of deep convection is impossible to justify within traditional cumulus-dynamics reasoning. The climatology of CIN is determined by a "boundary-layer quasiequilibrium" (Raymond 1995), in which surface fluxes are balanced by moist convective fluxes of θ_e. In this picture, the value of CIN is maintained near the value of turbulent kinetic energy characterizing the boundary layer circulations that form the roots of cumulus clouds. Boundary layer eddies capable of overcoming CIN are thus not rare, as proven by the ubiquity of cumulus clouds. If deep convection is viewed as simply being giant cumulus clouds, within the entraining-plume paradigm, then any sounding that supports small buoyant cumuli (with high entrainment rates) is unlikely to significantly inhibit cumulonimbi (which, owing to their larger diameter, have lower entrainment rates).

The flaw in this cumulus plume-oriented reasoning may lie in the observed fact that the vast majority of tropical rain falls from deep convection that is organized on the mesoscale (Rickenbach and Rutledge 1998 and references therein). Although isolated cumulonimbi do form spontaneously at the upper tail of the distribution of cumulus clouds, organized convection requires special initiation processes. Over the tropical oceans, this initiation process usually involves outflows from prior organized convection. Perhaps this sounds circular, or evasive of original causes, but the present model demonstrates that well-behaved, realistic large-scale convection variations may be produced (or amplified) in this way. The fact that almost all deep convection is triggered by prior deep convection may be inconvenient theoretically, but it is quite firmly founded in observation (e.g., Kingsmill and Houze 1999 and many others).

It may seem surprising that the subgrid-scale triggering energy generation effects of convection can outweigh its negative thermodynamic effects on the boundary layer. Many models with parameterized convection include the thermodynamic effects of downdrafts, but few, if any, include its effects on the generation of subsequent convection. Has a whole generation of cumulus parameterizations focused on the smaller of the two effects of downdrafts? Consider a prototype organized convective system: the 2D squall line. Squalls are frequently observed to sweep through regions previously containing only shallow cumuli, proving the susceptibility of those regions to deep convection if it is appropriately triggered.

Cloud-resolving models have shown that a statistically steady squall line can propagate indefinitely through a conditionally unstable environment (e.g., Fovell and Ogura 1988). Let us divide a region containing such a squall line into two large-scale boxes. The box ahead of the line is undisturbed, while the other contains the squall line. The undisturbed box has a higher box mean boundary layer θ_e, while the box containing the line has a lower θ_e, which is furthermore subject to a negative tendency due to the continuing effects of the squall line's downdrafts. Nonetheless, the gust front generated by the squall line causes it to persist in the box in which it already exists. In this case, it is clear that the triggering effect of convective downdrafts is more important to the evolution of the large scales of the convection field than is the large-scale (area average) θ_e tendency due to those same downdrafts. Would the more typical situation of an ensemble of unsteady mesoscale convective line segments be qualitatively different?

The model deep convection's dependence on subgrid-scale triggering energy introduces hysteresis into the relationships between convection and thermodynamic variables alone (CAPE, CIN, θ_e). Since observational studies of such relationships usually indicate weak or ambiguous dependences, this hysteresis may be (rather weakly) viewed as realistic. More importantly, the K dependence of convection amplifies the convective variability generated by thermodynamic fluctuations. If deep convection begets more deep convection, then even temperature waves of $<1°C$ amplitude can cause the

system to transition between undisturbed and disturbed states (Fig. 10). This too may be viewed as realistic.

This model invokes a single scalar K as the "temperature" characterizing the statistical vigor of subgrid-scale fluctuations, or "triggering energy." Other treatments of subgrid-scale convective initiation dynamics have been considered recently. Qian et al. (1998) divide each grid box in a large-scale model into preconvective and postconvective ("wake") parts, with assumptions about wake geometry to predict how much of the box is "swept" by gust fronts per unit time. Ridout and Reynolds (1998) invoke the idea that boundary layer thermals are the triggers for deep-convective clouds, to introduce a boundary layer Richardson number dependence into a GCM convective closure. Pan and Randall (1998) developed a prognostic closure which, although it ignores convective inhibition and initiation dynamics, does involve a heuristic budget for subgrid-scale energy ("cumulus kinetic energy"). Statistical description of subgrid-scale variability with more degrees of freedom could be considered, if enough observational evidence existed to fit additional parameters. The present simple treatment seems to fit our low level of systematic understanding of initiation processes in organized deep-convective cloud ensembles.

In this model, the second internal mode, with its strong influence on CIN and hence convection, governs the propagation speed of the unstable waves. Because moisture is concentrated in the lowest part of the troposphere, moisture-convergence convection closures also give a special importance to high vertical wavenumbers (Lindzen 1974; Chang and Lim 1988; Cho and Pendlebury 1997). Oouchi (1999) found that the second internal mode plays a critical role in generating the hierarchy of westward-moving cloud clusters inside eastward-moving superclusters in a 2D cloud resolving model. Haertel and Johnson (1998) interpreted observations of 2-day westward-moving convection waves in the COARE data in a manner very consistent with the formulation of this model. In particular, the variation of convection across the wave was seen as a consequence of CIN variation due to second-mode temperature structure.

The vertical structure of the waves in this model is merely ornamented by the deep forced response of the first internal mode. In terms of temperature, this forced response is in quadrature with the second-internal-mode temperature variations, and the resulting convective variations. The result is a tilted phase structure, as in observations. In the linearized two-mode dynamics here, each mode has independent energetics. The concept of vertical propagation of energy (by which tilted phase structure in atmospheric waves is usually interpreted) is difficult to apply. Some discussion of the relationship between vertical-mode and vertical-propagation thinking may be found in the appendix of Mapes (1998), but there is a need for further theoretical illumination.

Many of the variables in this model exhibit quasi-

equilibria with each other, since the wave periods are long compared to the small (few hour) lags that characterize the convective processes. Even if a quasi-equilibrium relationship between subgrid-scale variability and large-scale fields holds to accuracies far better than observations can ever hope to achieve, that relationship may fail badly as a parameterization scheme (Fig. 11) if it misrepresents the real causal relationships at work, as evidenced in small time lags (cf. Emanuel 1993).

The treatment of shallow convection is a key issue, even in models (such as this) that attempt to address only the more dramatic variability of deep convection. The structure of the low-level inhibition layer, and of lower-tropospheric humidity (the water supply to deep convection, variations of which are ignored here), depend crucially on shallow convection. Precipitating shallow- and middepth-convective clouds counter radiative cooling in the lower half of the troposphere, complementing the top-heavy heating profile of deep-convective cloud systems, which in turn excites the second internal mode that organizes the convection. An awkward aspect of this model, reflecting a true deficiency in the author's current understanding of the atmosphere, is that the shallow and deep convection, despite this close interrelationship, are treated separately. Nonetheless, this model's construction seems to me truer in an empirical sense than would an attempt to enforce a simple mechanistic unity on all moist-convective phenomena (e.g., as plumes with different entrainment rates).

This model assumes that shallow convection is ubiquitous and efficient in transporting the nonwake-recovery portion of the surface moisture flux up into a deep layer of the troposphere. This assumption is based on studies of boundary layers over the tropical oceans in the absence of deep convection (reviewed in LeMone 1995). In such a view, wind-induced surface heat flux enhancements (the WISHE mechanism; Emanuel 1987) would not necessarily lead to local *deep*-convection enhancements. Specifying the layer over which surface fluxes converge is a major point of uncertainty in WISHE theories. This is one reason the WISHE mechanism was excluded from this model for the present.

A novel aspect of this model is its recognition (however crude) of the fundamental importance of precipitation from cumulus congestus clouds, which span only the lower half of the troposphere. This part of the tropical cloud spectrum has received renewed attention in recent years (e.g., Johnson et al. 1999). Here these clouds are considered ubiquitous, but linearly modulated by lower-tropospheric temperature, supported by the observed fact (DeMott and Rutledge 1998) that their rain production varies less than that of deep convection, but in the same sense. In the model, congestus rain would therefore increase steadily in the hours leading up to an outbreak of deep convection (~antiproportional to the CIN curve in Fig. 10), in accord with field experience.

In summary, the physics considered here produce re-

alistic waves and reflect aspects of field experience of convection that are ignored entirely or not treated well in current global circulation models (GCMs). It is suggested that principles of the convective closure used here are applicable to models of any complexity level, and that stratiform instability may be one key to the problem of too little variability of deep convection in many GCMs. Future improvements to this toy model should include prognostic, advected humidity; appropriate convective momentum damping; and more realistic geometries and boundary conditions. Attempts are also being made to introduce a convective inhibition dependence, and a variable convection-triggering energy field, to the convection closure in the National Center for Atmospheric Research Community Climate Model (CCM3).

APPENDIX

Formal Interpretation of Fig. 1

The existence of shallow-convective heating processes that are more ubiquitous (less spatially concentrated) than deep convection may be deduced from large-scale observations, using a hydrostatic pressure-coordinate budget of dry static energy $s = C_p T + gz$, with notations following Yanai et al. (1973):

$$\frac{\partial s}{\partial t} + \nabla \cdot (s\mathbf{V}_h) + \frac{\partial}{\partial p}(s\omega) = R + L, \quad \text{(A1)}$$

where R is radiative heating and L is net latent heating. We idealize the tropical atmosphere as a closed system, divisible into two complementary regions: regions without deep convection (subscript N) and deep-convective regions (subscript D). Definitions of these regions depend on resolution and will be selected based on the scales at which observations are available. Averaging (A1) over region N, and discarding time variations and small horizontal transport terms, yields

$$\overline{\omega}_N \frac{\partial \overline{s}_N}{\partial p} = \overline{R}_N + \overline{L}_N - \frac{\partial}{\partial p}\overline{(s'\omega')} \equiv \overline{R}_N + \overline{C}_N, \quad \text{(A2)}$$

where the overbar denotes the spatial average and the prime denotes deviations from that average. The convective heating, C, is the sum of latent heating L and vertical eddy flux convergence.

Since N and D are complementary regions of a closed system, $\overline{\omega}_N = -\sigma\overline{\omega}_D$, by mass continuity, where σ is the ratio between the areas of regions D and N. If we also assume that $\overline{s}_D = \overline{s}_N$, then (A2) becomes

$$\overline{C}_N = -\overline{R}_N - \sigma\overline{\omega}_D \frac{\partial \overline{s}_D}{\partial p} = -\overline{R}_N - \sigma\overline{Q}_{1D}, \quad \text{(A3)}$$

where the second equality introduces Q_1, Yanai et al.'s (1973) "apparent heat source," averaged over the deep-convective region D, again neglecting time changes and small horizontal transport terms. Finally, it is convenient to cast the budget in terms of the tropical mean radiative heating $\overline{R}$:

$$\overline{C}_N = -\overline{R} - \sigma(\overline{Q}_{1D} - \overline{R}_D) \quad \text{(A4)}$$

Estimates of the terms on the rhs of (A4), divided by heat capacity C_p, are plotted in Fig. 1. Bergman and Hendon's (1998, hereafter BH98) all-Tropics (20°N–20°S) mean radiative heating profile, computed using satellite-observed cloudiness and humidity analyses in a radiative transfer model, is plotted on the left (negative). Radiation cools the troposphere by 1°–2° per day, with some structure associated mainly with cloud distributions. In particular, the maximum cooling at 750 mb is associated with cloud tops over the colder areas of the tropical oceans, while the warm-ocean mean profile is more constant with height. The present argument does not rest upon that level of detail.

Three observational estimates of deep-convective-region heating $\sigma(\overline{Q}_{1D} - \overline{R}_D)$ are plotted on the right (positive). On the earth, deep convection is concentrated both climatologically, by time mean geographical and SST patterns, and by transient disturbances. To obtain observational estimates for N–D partitions at two radically different resolutions, we will utilize both types of deep-convective variability.

The two broken lines were derived from 120-day mean Q_1 profiles from COARE rawinsonde arrays: the intensive flux array (IFA; $\sim$2.5 × 10^5 km^2, dotted) and the outer sounding array (OSA; $\sim$10 times larger, dashed). These profiles were provided by P. Ciesielski and R. H. Johnson (1998, personal communication) and include slight data corrections unavailable to Lin and Johnson (1996b). The solid line was derived from a Q_1 estimate based on MH95's airborne Doppler radar data obtained inside the rain areas of 10 COARE mesoscale convective systems (MCSs). Time mean radiative heating profiles for the Indo-Pacific convective region (10°N–10°S, 100°E–180°, from the calculations described in BH98) were idealized as −1.1 K d^{-1} below the 300-hPa level, linearly increasing to +1.1 K d^{-1} at 150 hPa.

The area fractions σ (0.25 for the rawinsonde-array profiles, 0.01 for the Doppler radar profile) used to scale the profiles in Fig. 1 were chosen to minimize the residual $\overline{C}_N$ in the upper troposphere, based on the definition of N as being "non-deep-convective" regions. The implied picture is that the time mean IFA–OSA Q_1 profiles are representative of some 20% of the Tropics

in which all the deep-convective heating is concentrated in the time mean. Likewise, the Q_1 profiles of the radar-observed rain areas are assumed to be representative of 1% of the Tropics, in which all the deep-convective heating is concentrated when one looks at the atmosphere with mesoscale resolution at a particular moment.

According to (A4), the residuum (sum) of the profiles of Fig. 1 is $\overline{C}_N$, convective heating in non-deep-convective regions. This shallow-convective heating includes both eddy heat flux convergence and net condensation heating in shallow-cumulus showers. The sum of the two solid lines in Fig. 1 indicates that this shallow-convective heating occurs almost totally outside the rain area of MCSs. The smaller sums of the radiation curve and the broken lines in Fig. 1 imply that shallow-convective heating is less completely excluded from the time mean IFA and OSA heating processes, but the implied shallow convective heating profile is similar, extending up to the midtroposphere. This vertical extent, and the magnitude, indicate that condensation in showers with midtropospheric tops is an important part of the budget. In short, shallow-convective heating is distinct from deep MCS heating and is much less variable. It is ubiquitous on large scales, occurring both inside and outside of the regions (both climatological and transient) in which deep convection is highly concentrated.

Although Q_1 profiles from deep-convective regions with less top-heavy profiles do exist, for example, in the Atlantic ITCZ (Frank 1983), it remains true, more generally, that Q_1 profiles of deep-convective regions never indicate enough dry static energy export in the lowermost tropical troposphere to obviate the need for shallow-convective heating outside these regions (cf. Gray 1973). In the subcloud layer in particular, shallow-convective heating occurs literally almost everywhere, since large-scale dry static energy export is nearly impossible in such a thin, neutrally stratified layer.

REFERENCES

Addis, R. P., M. Garstang, and G. D. Emmitt, 1984: Downdrafts from tropical ocean cumuli. *Bound.-Layer Meteor.,* **28,** 23–49.
Allen, S. J., and R. A. Vincent, 1995: Gravity wave activity in the lower atmosphere: Seasonal and latitudinal variations. *J. Geophys. Res.,* **100,** 1327–1350.
Bergman, J. W., and H. H. Hendon, 1998: Calculating monthly radiative fluxes and heating rates from monthly cloud observations. *J. Atmos. Sci.,* **55,** 3471–3491.
Chang, C.-P., and H. Lim, 1988: Kelvin wave-CISK: A possible mechanism for the 30–50 day oscillations. *J. Atmos. Sci.,* **45,** 1709–1720.
Chao, W. C., and S.-J. Lin, 1994: Tropical intraseasonal oscillation, super cloud clusters, and cumulus convection schemes. *J. Atmos. Sci.,* **51,** 1282–1297.
Cho, H.-R., and D. Pendlebury, 1997: Wave CISK of equatorial waves and the vertical distribution of cumulus heating. *J. Atmos. Sci.,* **54,** 2429–2440.
DeMott, C. A., and S. A. Rutledge, 1998: The vertical structure of TOGA COARE convection. Part II: Modulating influences and implications for diabatic heating. *J. Atmos. Sci.,* **55,** 2748–2762.
Emanuel, K. A., 1987: An air–sea interaction model of intraseasonal oscillations in the Tropics. *J. Atmos. Sci.,* **44,** 2324–2340.

——, 1993: The effect of convective response times on WISHE modes. *J. Atmos. Sci.,* **50,** 1763–1775.
——, J. D. Neelin, and C. S. Bretherton, 1994: On large-scale circulations in convecting atmospheres. *Quart. J. Roy. Meteor. Soc.,* **120,** 1111–1143.
Fovell, R. G., and Y. Ogura, 1988: Numerical simulation of a midlatitude squall-line in two dimensions, *J. Atmos. Sci.,* **45,** 3846–3879.
Frank, W. M., 1983: The structure and energetics of the eastern Atlantic intertropical convergence zone. *J. Atmos. Sci.,* **40,** 1916–1929.
Fulton, S. R., and W. H. Schubert, 1985: Vertical normal mode transforms: Theory and application. *Mon. Wea. Rev.,* **113,** 647–658.
Godfrey, J. S., R. A. Houze Jr., R. H. Johnson, R. Lukas, J.-L. Redelberger, A. Sumi, and R. Weller, 1998: The Coupled Ocean Atmosphere Response Experiment (COARE): An interim report. *J. Geophys. Res.,* **103,** 14 395–14 450.
Gray, W. M., 1973: Cumulus convection and larger scale circulations: I. Broadscale and mesoscale considerations. *Mon. Wea. Rev.,* **101,** 839–855.
Haertel, P. T., and R. H. Johnson, 1998: Two-day disturbances in the equatorial western Pacific. *Quart. J. Roy. Meteor. Soc.,* **124,** 615–636.
Houze, R. A., Jr., 1997: Stratiform precipitation in regions of convection: A meteorological paradox? *Bull. Amer. Meteor. Soc.,* **78,** 2179–2196.
——, and C. Cheng, 1977: Radar characteristics of tropical convection observed during GATE: Mean properties and trends over the summer season. *Mon. Wea. Rev.,* **105,** 964–980.
Johnson, R. H., T. M. Rickenbach, S. A. Rutledge, P. E. Ciesielski, and W. H. Schubert, 1999: Trimodal characteristics of tropical convection. *J. Climate,* **12,** 2397–2418.
Kingsmill, D. E., and R. A. Houze Jr., 1999: Thermodynamic characteristics of air flowing into and out of convection over the west Pacific warm pool. *Quart. J. Roy. Meteor. Soc.,* **125,** 1209–1229.
LeMone, M. A., 1995: The cumulus-topped boundary layer over the ocean. *Proc. NCAR Summer Workshop on the PBL,* Boulder, CO, National Center for Atmospheric Research, 121–138.
——, and R. J. Meitin, 1984: Three examples of fair-weather mesoscale boundary layer convection in the Tropics. *Mon. Wea. Rev.,* **112,** 1985–1997.
Lin, X., and R. H. Johnson, 1996a: Kinematic and thermodynamic characteristics of the flow over the western Pacific warm pool during TOGA COARE. *J. Atmos. Sci.,* **53,** 695–715.
——, and ——, 1996b: Heating, moistening, and rainfall over the western Pacific warm pool during TOGA COARE. *J. Atmos. Sci.,* **53,** 3367–3383.
Lindzen, R. S., 1974: Wave-CISK in the Tropics. *J. Atmos. Sci.,* **31,** 156–179.
Mapes, B. E., 1997a: What controls large-scale variations of deep convection? *Proc. New Insights and Approaches to Cumulus Parameterization,* Reading, United Kingdom, ECMWF, 157–165.
——, 1997b: Equilibrium vs. activation controls on large-scale variations of tropical deep convection. *The Physics and Parameterization of Moist Convection,* R. K. Smiths, Ed., Kluwer Academic, 321–358.
——, 1998: The large-scale part of tropical mesoscale convective system circulations: A linear vertical spectral band model. *J. Meteor. Soc. Japan,* **76,** 29–55.
——, and R. A. Houze Jr., 1995: Diabatic divergence profiles in western Pacific mesoscale convective systems. *J. Atmos. Sci.,* **52,** 1807–1828.
——, and P. Zuidema, 1996: Radiative–dynamical consequences of dry tongues in the tropical troposphere. *J. Atmos. Sci.,* **53,** 620–638.
Nitta, T., 1970: Statistical study of tropospheric wave disturbances in the tropical Pacific region. *J. Meteor. Soc. Japan,* **48,** 47–59.
Oouchi, K., 1999: Hierarchical organization of super could cluster

caused by WISHE, convectively induced gravity waves, and cold pool. *J. Meteor. Soc. Japan,* **77,** 907–927.

Pan, D.-M., and D. A. Randall, 1998: A cumulus parameterization with a prognostic closure. *Quart. J. Roy. Meteor. Soc.,* **124,** 949–981.

Peixoto, J. P., and A. H. Oort, 1992: *Physics of Climate.* American Institute of Physics, 520 pp.

Qian, L., G. S. Young, and W. M. Frank, 1998: A convective wake parameterization scheme for use in general circulation models. *Mon. Wea. Rev.,* **126,** 456–469.

Raymond, D. J., 1994: Convective processes and tropical atmospheric circulations. *Quart. J. Roy. Meteor. Soc.,* **120,** 1431–1455.

——, 1995: Regulation of moist convection over the west Pacific warm pool. *J. Atmos. Sci.,* **52,** 3945–3959.

——, and D. J. Torres, 1998: Fundamental moist modes of the equatorial troposphere. *J. Atmos. Sci.,* **55,** 1771–1790.

Rickenbach, T. M., and S. A. Rutledge, 1998: Convection in TOGA COARE: Horizontal scale, morphology, and rainfall production. *J. Atmos. Sci.,* **55,** 2715–2729.

Ridout, J. A., and C. A. Reynolds, 1998: Western Pacific warm pool region sensitivity to convective triggering by boundary layer thermals in the NOGAPS atmospheric GCM. *J. Climate,* **11,** 1553– 1573.

Spencer, R. W., and J. R. Christy, 1992: Precision and radiosonde validation of satellite gridpoint temperature anomalies. Part II: A tropospheric retrieval and trends during 1979–90. *J. Climate,* **5,** 858–866.

Takayabu, Y. N., 1994: Large-scale cloud disturbances associated with equatorial waves. Part I: Spectral features of the cloud disturbances. *J. Meteor. Soc. Japan,* **72,** 433–448.

Warren, S. G., C. J. Hahn, J. London, R. M. Chervin, and R. L. Jenne, 1988: Global distribution of total cloud cover and cloud type amounts over the ocean. NCAR Tech. Note NCAR/TN-317+STR, 41 pp. and 170 maps.

Wheeler, M., and G. N. Kiladis, 1999: Convectively coupled equatorial waves: Analysis of clouds and temperature in the wavenumber–frequency domain. *J. Atmos. Sci.,* **56,** 374–399.

——, ——, and P. J. Webster, 2000: Large-scale dynamical fields associated with convectively coupled equatorial waves. *J. Atmos. Sci.,* **57,** 613–640.

Yanai, M., S. K. Esbensen, and J.-H. Chu, 1973: Determination of bulk properties of tropical cloud clusters from large-scale heat and moisture budgets. *J. Atmos. Sci.,* **30,** 611–627.

Yano, J.-I., J. C. McWilliams, M. W. Moncrieff, and K. A. Emanuel, 1995: Hierarchical tropical cloud systems in an analog shallow-water model. *J. Atmos. Sci.,* **52,** 1723–1742.

——, M. W. Moncrieff, and J. C. McWilliams, 1998: Linear stability and single-column analyses of several cumulus parameterization categories in a shallow-water model. *Quart. J. Roy. Meteor. Soc.,* **124,** 983–1005.

Young, G. S., S. M. Perugini, and C. W. Fairall, 1995: Convective wakes in the equatorial Pacific during TOGA. *Mon. Wea. Rev.,* **123,** 110–123.

Yu, J.-Y., C. Chou, and J. D. Neelin, 1998: Estimating the gross moist stability of the tropical atmosphere. *J. Atmos. Sci.,* **55,** 1354–1372.

Zipser, E. J., 1977: Mesoscale and convective-scale downdrafts as distinct components of squall-line structure. *Mon. Wea. Rev.,* **105,** 1568–1589.